Wesleyan University | The Honors College

Mapping the Local Interstellar Medium: Using Hubble to Look Back at the ISM Along the Sun's Historical Trajectory

by

Hunter Vannier
Class of 2020

A thesis submitted to the
faculty of Wesleyan University
in partial fulfillment of the requirements for the
Degree of Bachelor of Arts
with Departmental Honors in Astronomy

Middletown, Connecticut | April, 2020

All we have to decide is what to do with the time that is given to us.

–J.R.R. Tolkien

The Lord of the Rings: The Fellowship of the Ring

Acknowledgements

I would first like to express my sincerest gratitude to my fellow VVO basement dwellers, especially T.G, B.M., G.G., and my ISM buddy F.K. I am so thankful for your support and encouragement, and most importantly your friendship. Even though our time together was cut short, I will hold the memories we shared dear to me for the rest of my life. I cannot imagine my time at Wes without you.

Next, I need to thank my advisor Seth Redfield for the incredible support he has given me since freshman year. You will always be a role model to me not only because of the high standards you hold yourself to as a scientist, but also for the care and time you commit to teaching, inspiring numerous students to love the cosmos along the way (guilty). The true kindness and empathy you have shown me over the past four years have made this experience so much more worthwhile.

Finally, I would like to thank my parents. Your unflinching love, support, and sacrifice have enabled me to pursue and continue to pursue my dreams no matter where they take me, and I am so lucky to have you as parents.

I love you.

Contents

Chapter 1

Introduction

The history of our Sun's travel through the Milky Way is a dynamic one. As our solar system pushes headlong through the galaxy, it encounters diverse environments of interstellar medium (ISM); clouds of gas, dust, ionized particles and cosmic rays that exist in the empty space between different star systems. The ISM is a fundamental component in galactic evolution. Supernovae eviscerate stars and blast the stellar materials outward to be recycled by the Galaxy. Eventually, pockets of ISM form from the supernovae remnants and become dense enough to collapse and form stars and planets, setting the cycle anew. The diverse environments from which clouds develop cause them to have varying elemental composition, radial velocity, temperature, turbulence, and densities. All the while, our solar system travels through these varying environments. At the interface between these encounters is the heliosphere, a "protective bubble" that surrounds our solar system, created when the Sun's outward moving fully ionized solar wind balances the inward pressure of the ISM, forming a low density cavity in the ISM in the direction of the Sun's travel (Muller et al. 2006). As the heliosphere is highly sensitive to change in its interstellar environment, it is likely that its size and structure has changed with time (Zank & Frisch 1999; Frisch 2006; Muller et al. 2006).

For almost a century, researchers have speculated that Galactic conditions are

intertwined with the Earth's climate. In the 1920's, Harlow Shapley postulated that variations in the Galactic environment may affect the atmosphere of our planet and that a significant increase in solar radiation could bring about major climate change events because of the impact of the Sun's passage through changing interstellar environments (Shapley 1921).

Still today, the connection between our solar system and its Galactic environment is of great scientific interest (Muller et al. 2006; Frisch 2006; Frisch et al. 2013). An encounter with a sufficiently dense cloud of ISM could cause the heliosphere to be compressed, exposing the inner solar system to higher levels of Galactic cosmic rays and dust deposition (Frisch 2006). As both theoretical models and the velocity structure of the LISM support the idea that the Sun passes through these cloudlets on geologically short time scales of $\leq 10^4$--10^5 years (Muller et al. 2006), it is feasible that fluctuations in the interstellar environment may even be detectable in the geological records of the Earth or solar system bodies. Without heliospheric protection, the Earth would receive an influx of cosmic rays, greatly increasing the creation of secondary particles and natural radiation that occurs when rays interact with the Earth's atmosphere (Redfield 2006). Analysis of deep sea sediment core samples show evidence of many unexplained influxes of cosmic radiation over the past $\sim$65 million years, but the most reliable dating covers the past $\sim$5 million years (Zachos et al. 2001). By reconstructing the interstellar environment of our most recent past, we can compare the fluctuations in Earth's geological record to a potential encounter with a high density cloud in the LISM.

1.1 The Interstellar Medium

Inhabiting the void between different star systems are clouds of gas and dust which we refer to as the interstellar medium. The classical model of the ISM is described by three components: cold ($T \leq 50$ K) neutral and molecular gas, warm neutral or partially ionized gas (10^4 K), and million-degree, low-density fully ionized plasma (McKee & Ostriker 1977). It was thought that each of these different regions maintained thermal and pressure equilibrium. However, simulations of the nearest, most recent supernovae explosions in thermally evolving, inhomogeneous background ISM predict that no pressure or thermal equilibrium would be possible (Breitschwerdt & de Avillez 2006). Models of supernovae explosion at the Galactic rate predict turbulent interstellar gas with varying temperatures (de Avillez & Breitschwerdt 2007), results also supporting that the ISM is not in equilibrium.

1.1.1 The Local Bubble

As Frisch et al. (2011) so aptly describe it, the local interstellar medium (LISM) is the screen through which we view the rest of the Universe.

We currently reside in the Local Bubble (LB), which is located in the Local Orion Arm of the Milky Way (Lallement et al. 2003). The LB is an area generally composed of low density hot plasma ($10^{5.65}$--10^6 K) that extends 70--200 pc from the Sun. The structure of the Local Bubble is evident from observations of color excess maps showing a hole in the interstellar dust around the Sun, in conjunction with observations of soft X-ray background (SXRB) radiation covering the sky (Frisch et al. 2011). In Figure 1.1, the extinction of stars within 50 pc of the

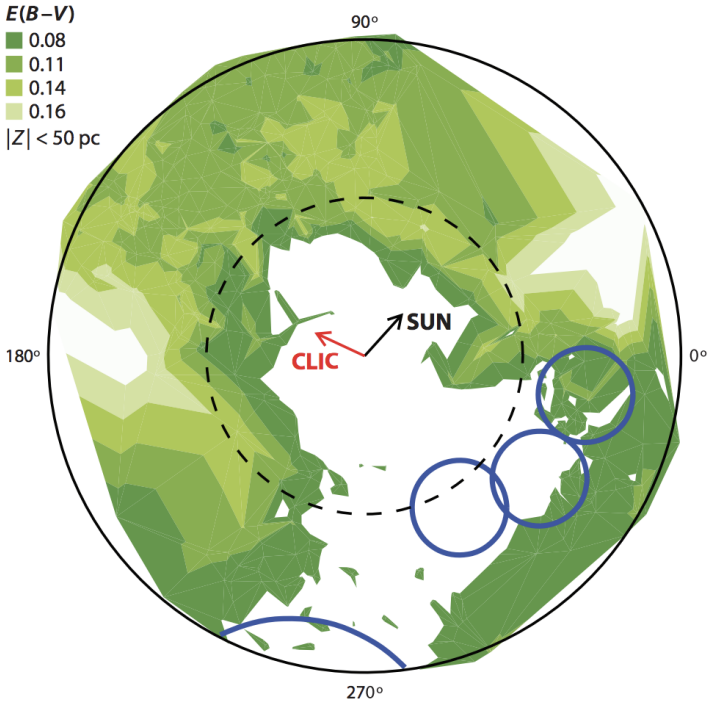

Figure 1.1: The density of interstellar dust defines the boundary of the Local Bubble, established with color excess *E(B-V)* data from the Hipparcos catalog (Perryman et al. 1997). The density disparity is made clear by the edge between the green (high density) and white (low density) regions contained within the dashed circle (radius∼100 pc). Arrows represent the vector motions of the cluster of local interstellar clouds (CLIC) (red) and the Sun (black). The motions are almost perpendicular to one another. Three large blue circles show the three subgroups of the Sco-Cen Association, the nearest 0B-star association whose stellar winds may be responsible for creating the Local Bubble; the blue arc at $\sim 270°$ corresponds to the Gum Nebula. From Frisch et al. (2011).

Galactic plane shows the structure of the Local Bubble. The abrupt border of the higher density, dusty region around 100 pc highlights the significant difference in density between it and the white lower density plasma in which we currently reside. The walls of the Local Bubble boundary have a minimum column density of $N(\mathrm{H}) > 10^{20.65}$ cm^{-2} (Frisch et al. 2011).

We can likely attribute the creation of the Local Bubble to supernovae explosions or strong stellar winds. Both are highly energetic processes capable of carving out such a large, low density region. Multiple studies connect the move-

ment of stars from the Scorpius-Centaurus Association (See Figure 1.1), into the Local Bubble 10--15 Myr ago (Frisch et al. 2011; Frisch 1995; Fuchs et al. 2006).

Zooming in further on our interstellar environment reveals evidence of complex and dynamic small-scale structures surrounding the Sun. Traversing this diverse environment has a significant effect on our solar system. Indeed, quantifying the traversal of the solar system through the LISM is the main goal of this thesis.

1.1.2 The Local Interstellar Medium

As Frisch et al. (2011) so aptly describe it, the local interstellar medium (LISM) is the screen through which we view the rest of the Universe. In recent times, the advent of high-resolution UV spectra from *HST* has made it possible to characterize the morphology of the closest clouds of interstellar gas. Surrounding the Sun is a network of warm (5,000--10,000 K) partially ionized gas clouds, extending a distance of about 15 parsecs (Linsky et al. 2019). Analyzing high spectral resolution data along sight lines to stars in various directions has revealed a diverse environment with various velocity components (Müller et al. 2009). In their analysis of over 150 sight lines spanning a wide range of sky, Redfield & Linsky (2008) peered through the screen of the LISM and identified 15 discrete clouds of warm interstellar gas. Figure 1.2 shows the different clouds, each labeled and color coded to distinguish borders and projected in Galactic coordinates.

Reconstructing a cloud of ISM begins with examining emission lines that appear at specific wavelengths in the stellar spectra. If cloud lies between us and a target star, it can absorb light based on its elemental composition and ionization state. We examine a wide range of emission lines and try to identify absorption due to ISM and not the inherent characteristics of stellar spectra. If an absorp-

tion feature is identified, physical characteristics associated with the cloud can be extracted such as temperature, turbulence, column density, and radial velocity. Redfield & Linsky (2008) recognised the clouds were discrete by identifying consistent velocity components throughout the numerous sight line measurements.

Based on their velocity measurements, the clouds move in the same general direction (Redfield & Linsky 2008; Linsky et al. 2019) which coincides with the direction of stellar wind from the nearest OB-star association, Sco-Cen (Frisch et al. 2011). Among the 15 clouds, the most important to this study are the ones which are closest and in the direction of past solar motion.

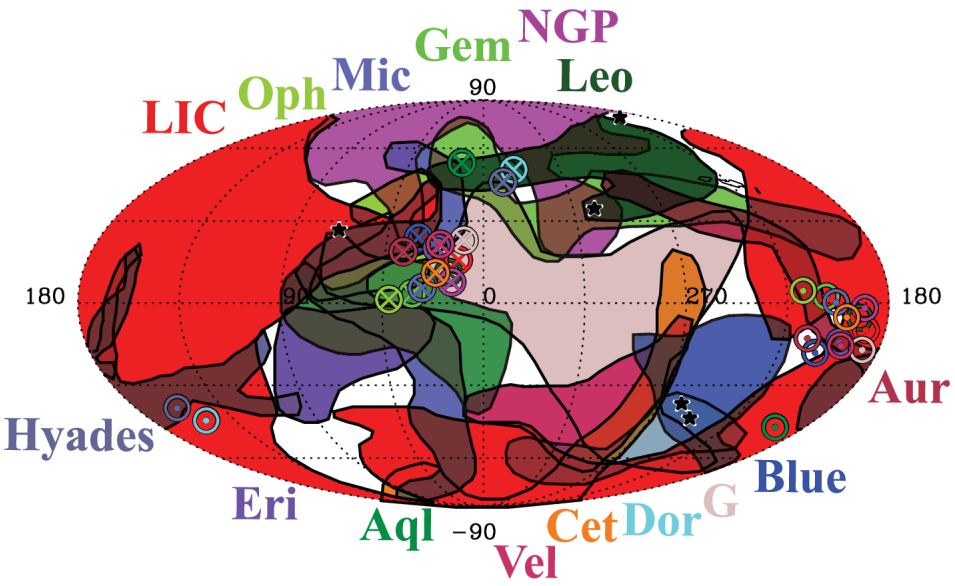

Figure 1.2: A map of the 15 clouds of ISM in close proximity to the Sun. Each has a different radial velocity vector based on observations of 157 sight lines. The LIC dominates over 50% of the sky and is the cloud we are most likely embedded in today. The circles with x's in the middle are in the upwind direction, and circles with dots in the middle are in the downwind direction. Upwind denotes the direction toward the nose of the heliosphere and downwind denotes the opposite direction. From Redfield & Linsky (2008)

1.1.3 The Inner LISM

.

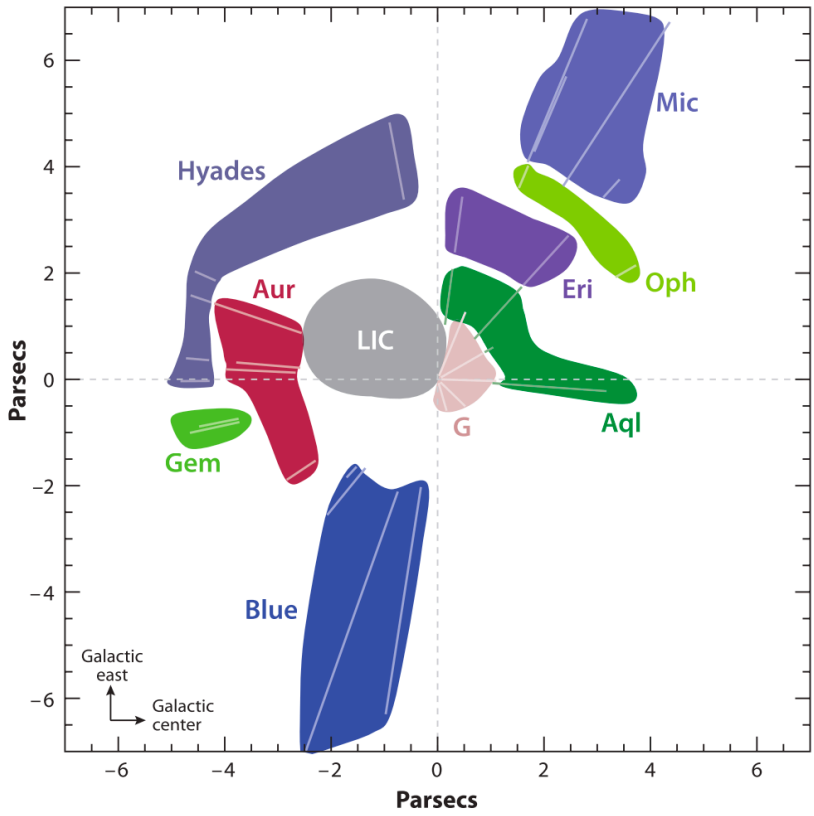

Figure 1.3: The nearest clouds of the LISM on the Galactic plane as viewed from Galactic north. The grey dashed lines intersect at the current position of the Sun. The Sun is at the border of the LIC and will likely exit the LIC soon and enter the G cloud. The LIC, Aur, and Blue clouds traverse or are near the path of past solar motion. From Frisch et al. (2011)

Of all the 15 clouds, the Local Interstellar Cloud (LIC) is special. Absorption from the Local Interstellar Cloud (LIC) appears in the numerous sight lines of all sky surveys to probe the LISM around us (Redfield & Linsky 2008; Malamut et al. 2014; Konow et al. 2020). This is made obvious by the red swath of the LIC occupying much of the map in Figure 1.2. Because we observe the LIC occupying so much of the sky, it is expected we are surrounded by LIC material

and as such it is our best candidate for evaluating the morphological details of the LISM (Linsky et al. 2019). Figure 1.3 shows the position of the LIC and the 10 clouds in closest proximity to the Sun. The intersection of the grey dashed line shows where the Sun is today; at the edge of the LIC. Additionally, the LIC velocity closely matches measurements of the inflow velocity of interstellar gas into the heliosphere, supporting the assertion we are within the LIC (McComas et al. 2015; Linsky et al. 2019).

Immersion in the LIC gives us the best opportunity to characterize the other clouds of the LISM. We can obtain column density measurements for the nearest clouds, but in order to determine the distance to their borders, we must know the volume density. Without in-situ measurements, this is a major problem, so we use the volume density of the LIC to estimate the edges of the other nearby clouds (Linsky et al. 2019).

Another byproduct of the numerous measurements of the LIC was the information which allowed the creation of a 3-D model. Figure 1.4 shows one the view of the LIC 3-D model from Galactic north, each contour representing a distance above or below the Galactic plane. Because the borders of the LIC are well constrained, this 3-D model gives us the best look at the finer structure and morphology of a cloud in the LISM (Redfield & Linsky 2000; Linsky et al. 2019).

A striking characteristic of the LIC is that in upwind direction, no LIC absorption is detected, implying that the Sun will exit the LIC in less than 3000 years (Redfield & Linsky 2008). The resulting change in the solar interstellar environment may have far reaching implications. Transitioning into a new material could change the velocity and density of the surrounding medium, in turn altering the boundary conditions of the heliosphere.

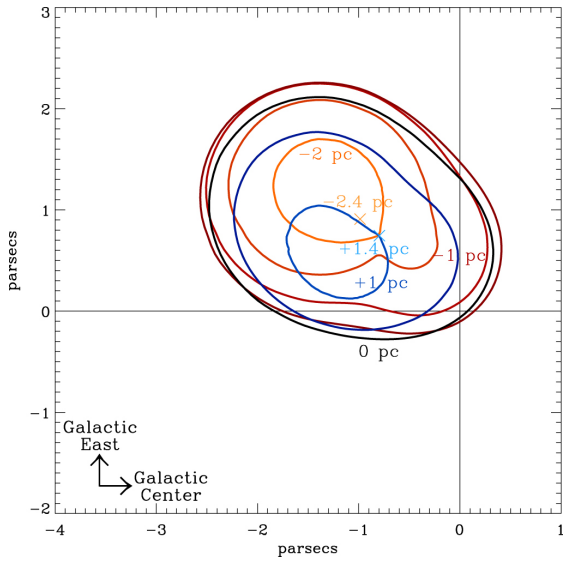

Figure 1.4: A contour map of the LIC from the view of the North Galactic Pole (Linsky et al. 2019), where the contours are parallel to the Galactic plane. The Sun is located at (0,0). The blue layers are cuts below to the Galactic plane, and red contours are above. The orange "x" represents where the edge of the LIC is furthest below the plane; the blue "x" above. From Linsky et al. (2019)

1.2 The Heliosphere

As our solar system journeys through the Milky Way, the Sun's outward moving solar wind carves out a cavity in the surrounding interstellar medium, forming the heliosphere. The solar magnetic field and a constant stream of charged particles emanating from the Sun deters material contained in the ISM from penetrating further into the solar system.

The boundary of the heliosphere is defined as the point where the momentum of inward moving interstellar material reaches an equilibrium with the opposing flow of solar wind. As the Sun moves through varying interstellar environments, the boundary conditions are mostly governed by the density and velocity of the clouds of ISM and the strength of the solar wind. A stronger solar wind could force the heliospheric boundary radially outward, and conversely a transition into

a dense, fast moving cloud could compress the boundary radially inward (Zank & Frisch 1999).

In order to attain a sense of orientation when describing the interaction between interstellar material and the heliosphere, the "upwind" direction is defined as directly opposite of the flow vector of the LISM cloud encountering the heliospheric boundary, and "downwind" is the direction opposite of this (Frisch 2006).

1.2.1 Structure

The heliosphere is formed when the outward moving solar wind carves out a low density bubble in the LISM in the direction of the Sun's velocity vector through the Milky Way (Frisch 2006). The interface between the LISM and the heliosphere in the upwind direction is comprised of three major components: the bowshock, heliopause, and termination shock. Extending radially from the Sun, contemporary distance estimates place these features at 285 AU, 148 AU, and 99 AU respectively. Figure 1.5 shows the orientation of these structural elements.

The first affect the ISM feels as it encounters the structure of the heliosphere is at the bowshock, where the interstellar gas is shocked and drastically slowed to subsonic speeds. One can imagine the bowshock as the wake pushed out in front of a ship as it travels through water. After being distorted and slowed by the bowshock, the interstellar material reaches a region called the outer heliosheath, just exterior to the heliopause.

The heliopause is the point at which the total solar wind and interstellar pressures reach an equilibrium (Frisch 2006), and check Holzer, 1989). On its journey away from the Sun, the solar wind has much of its kinetic energy converted to thermal energy, and slows from supersonic to subsonic velocities at the termina-

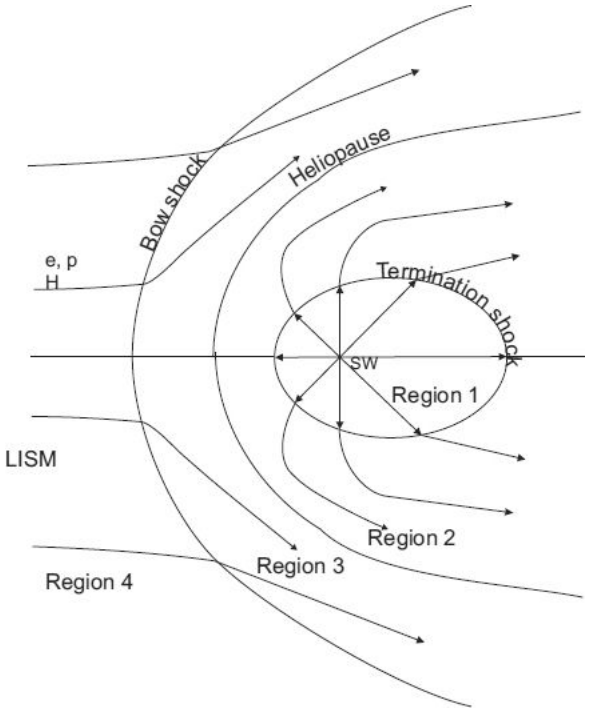

Figure 1.5: A schematic of heliospheric structure from Izmodenov et al. (2002). The arrows indicate the flow of neutral hydrogen from the interstellar medium and from the solar wind as it reaches the termination shock. The four regions are divided based on greatly different plasma properties: (1) supersonic solar wind, (2) subsonic solar wind in the heliosheath, (3) interstellar region of disturbed plasma surrounding the heliopause, (4) pristine, undisturbed ISM.

tion shock. The subsonic wind then enters a region between the termination shock and heliopause called the heliosheath (Frisch 2006; Izmodenov et al. 2002).

The *Voyager 1* mission spent much of its time in the heliosphere, and detected a large increase in interstellar plasma density after crossing the heliopause in 2012 (Gurnett et al. 2013). The longevity of *Voyager* enabled the unprecedented in-situ measurement of heliospheric structure and interstellar plasma.

The heliosphere can compress or expand reacting to a varying interstellar environment, changing the distance between the Sun these barrier features. As we will see later on, this directly affects the quantity of interstellar particles and cosmic rays entering the solar system.

As the Sun traverses varying environments of the LISM, the influx of particles into the solar system changes depending on the density and velocity of the clouds (Frisch 2006). Muller et al. (2006) model the change in heliospheric boundaries by varying interstellar parameters such as density, temperature, and velocity. Taking into account the distinct properties of major plasma regions related to the heliosphere (labeled in Figure 1.5), the model measures the response of the heliosphere to distinct interstellar environments. The model yielded heliopause distances as far as 400 AU and as close as 21 AU, an expansive range.

The absence of interstellar absorption at the predicted LIC velocity in the direction of the Suns motion implies, as stated earlier, that the Sun will leave the LIC in less than 3000 years (Redfield & Linsky 2008). Frisch et al. (2013) proposed that the inflow direction of interstellar material has changed over the last 40 years, suggesting that the heliospheres environment is changing in our lifetime.

1.2.2 Cosmic Rays and Earth

In the Sun's 220 million year orbit around the center of the Galaxy, it has experienced diverse environments such as dense molecular clouds, moderately dense clouds of ISM such as the one that currently surrounds the Sun, and extremely hot low density plasma. As we occupy different interstellar surroundings (Frisch & Mueller 2011), he size and particle content of the heliosphere is controlled by this interaction with the LISM.

A primary function of the heliosphere is the modulation of galactic cosmic rays (GCR's) our solar system encounters. If the Sun were to enter a cloud of ISM 50 times more dense than what we are surrounded by today, the termination

shock would move from ∼100 AU to ∼10 AU (Zank & Frisch 1999; Muller et al. 2006). This would drastically increase the amount of cosmic rays passing from the ISM through the heliosphere, enabling them to make their way into the inner solar system. (Muller et al. 2006). This is of great importance to Earth, as an increase of these energetic charged particles could have serious consequences for the environment and life forms on Earth. When GCR's interact with the atmosphere, a number of secondary particles are created, such as muons and electrons. A particle ray shower deposits muons in the lower atmosphere, which can cause cloud formation in the lower atmosphere (Carslaw et al. 2002). Increased cosmic ray flux would intensify cloud formation, which could lead to higher planetary albedo and a decrease in global temperature.

Another consequence of a high density cloud of LISM would be an increase in interstellar dust deposition into the Earth's upper atmosphere. Large amounts of interstellar dust could cause a reverse greenhouse effect. Infrared and thermal radiation would pass through the dust while visible light would be scattered (Pavlov et al. 2005).

Clearly, understanding our interstellar past can enable us to better understand possible past environmental conditions on the Earth.

1.3 Connecting to the Past

In order to reconstruct the most recent Galactic environment through which we've traveled, we must measure the LISM properties in the direction opposite of the Sun's current travel. Wyman & Redfield (2013) probed the ISM along the historical trajectory in order to understand the potential environments the Sun traversed and model the heliospheric expansion or contraction. They presented

an extensive sample of of 50 sight lines within 10° of the historical trajectory of the Sun. They examined high resolution spectra from ground based telescopes, analyzing the Ca II and Na II, the strongest optical transitions. However, due to spectral resolution limitations they were unable to detect the lowest interstellar column densities within 100 pc. Because they only resolved the more distant ISM, it is unlikely the Sun actually traversed those environments.

In this study, we attempt to establish a direct link between the contraction or expansion of the heliosphere and the Sun's travel through the LISM. Guided by the same principles as Wyman & Redfield (2013), we look at a sample of stars along the Sun's historical trajectory, but with the advantage of using high resolution UV spectra from *HST*. Almost all of the strongest resonance lines of the LISM are in the UV wavelength range, which we require in order to measure the low column densities in the LISM. The sensitivity of these lines enable us to accurately measure column densities of the nearest clouds, from which we can calculate distances to the cloud edges.

By analyzing a sample of nearby stars (<50 pc from the Sun), we resolve the complication of cloud movement that impacted Wyman & Redfield (2013). Simply, the nearest clouds of ISM haven't had much time to move since the Sun passed through them, so when we detect clouds in the spectra stars near the historical trajectory, we know that these clouds were actually there.

Because we know the velocity of both the Sun (Dehnen & Binney 1998) and clouds in the LISM (Redfield & Linsky 2008), in addition to the edges of the clouds along the historical trajectory of the Sun, we can combine them to reconstruct a timeline of the Sun's interaction with our most recent interstellar environment over the past ∼4--5 million years. We can then use this timeline to directly tie the potential expansion/contraction of the heliosphere to any effects an increase

in cosmic ray flux may have had on the inner solar system and Earth.

In the coming chapters, we analyze the sight lines of the most detailed sampling of any group of stars to date. We extract the physical properties of the closest LISM, giving us an unprecedented look at our actual past; a true, measurable connection between the Sun, solar system, and the interstellar environment through which we travel.

Chapter 2

Observations and Data

The goal of reconstructing our most recent interstellar environment requires a specific sample of stars, constrained both by distance from the Sun and proximity to the direction of past solar motion. This sample of stars is necessary in order to identify which constituents of the LISM lie on the path the Sun traversed.

2.1 Target stars

Our sample consists of eight stars that lie within ∼50 pc of our solar system and are chosen to have minimal angular separation from the direction of the Sun's historical trajectory, $l = 207.70°$ and $b = -32.41°$ (Dehnen & Binney 1998). At the Sun's current velocity in the Local Standard of Rest (LSR) (13.38 km s^{-1}) (Schönrich et al. 2010), the Sun would have traversed this distance over the past ∼4--5 million years. 50 pc is .01% of the circumference of the Sun's orbit around the center of the Milky Way, so we can approximate the Sun's path as a straight line over this distance.

Equally important is considering how the individual clouds of LISM have moved over this time. Targets are chosen to ensure the clouds have not had time to move out of the Sun's path. We can make this calculation based on the average cloud size (∼1.5 pc) (Redfield & Linsky 2000) and average transverse flow velocity (∼12.7 km s^{-1}) of cloudlets (Redfield & Linsky 2008).

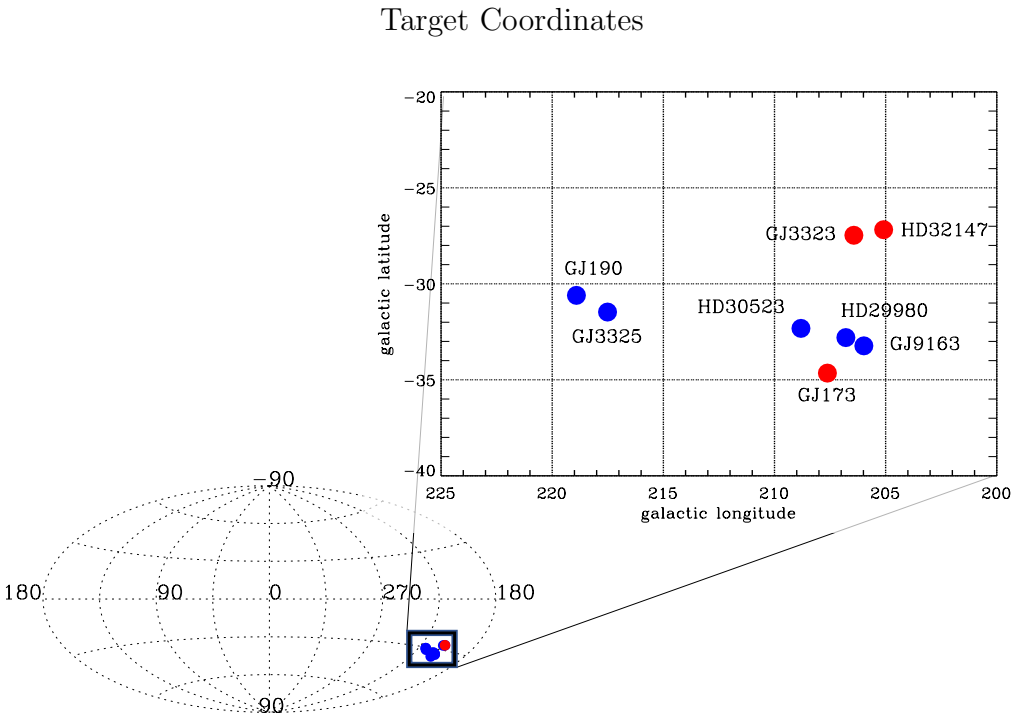

Figure 2.1: Our eight targets plotted in Galactic coordinates. The bottom left projection is a hammer projection of Galactic coordinates with the Galactic center in the middle, and the panel in the upper right zooms in on our eight targets. The blue dots show the stars we obtained observations for in the near-UV (1150--10300 Å), and the red dots mark the stars we observed in both the near-UV and far-UV (1150--1700 Å). They are tightly concentrated with minimal angular separation ($< 10°$) from the historical trajectory.

Table 2.1 lists the eight target stars, ordered by distance from the Sun. The closest stars have the largest angular separation from the historical trajectory because the Sun traversed these distances most recently, and the clouds have had less time to move. The targets are mostly late type stars with sufficient brightness to have high S/N LISM absorption spectrum. This proved to be particularly true for HD29980 and HD32147, G and K-type respectively. Their high S/N enabled the identification of two distinct ISM absorption profiles we used to educate the fits of some of the noisier spectra of other targets. Of the remaining stars, one is K-type and five are M-type.

Observations

Target	Data Set	Spectral Type	v_r (km/s)	l (deg)	b (deg)	Distance pc	$\Delta\theta$ (deg)
GJ3323	ocyw01010	M4.0Ve	39.417	206.43	-27.47	5.38	5.061
HD32147	ocyw02010	K3+V C	21.671	205.09	-27.18	8.85	5.70
GJ3325	ocyw03010	M3V C	15.34	217.51	-31.48	9.23	8.37
GJ190	ocyw04010	M3.5V C	33.9	218.91	-30.60	9.20	9.72
GJ173	ocyw0501	M1V C	-6.77	207.62	-34.65	11.214	2.24
GJ9163	ocyw0601	M0V C	10.3	205.98	-33.65	19.685	1.90
HD30523	ocyw07010	K5Vk C	27.27	208.81	-32.32	26.50	0.94
HD29980	ocyw08010	G3/5V D	32.33	206.80	-32.80	50.51	0.85

Table 2.1: All values are from the SIMBAD database unless specified otherwise. All distances were obtained from the GAIA DR2 release (Gaia Collaboration 2018). $\Delta\theta$ is the angular separation from the historical trajectory of the Sun, $l = 207.70$ and $b = -32.41$ (Dehnen & Binney 1998)

.

This tightly grouped sample of stars provides the most detailed observations of any local interstellar sight line to date, giving an unprecedented opportunity to study small-scale variations in the LISM. Resolving fine structural details of the LISM on such a short distance scale is not feasible with ground-based telescopes, so we use data from the *Hubble Space Telescope*, whose high resolution UV-spectorgraphs are ideal for the job.

2.2 Instrumentation and Observational Parameters

The data for this project were obtained from the Space Telescope Imaging Spectograph (STIS) aboard the *Hubble Space Telescope* (*HST*). The STIS offers a wide spectral range (1150--10300 Å) for observation, making it an instrument useful for numerous astrophysical applications. It is particularly useful for ISM because it encompasses spectral region of far UV (FUV) and near UV (NUV).

The high spectral resolving power of $R \approx 114,000$ (where $R = \frac{\lambda}{\delta\lambda}$) data across this range is essential in resolving the strongest resonance lines in areas of low column density that exist in the LISM.

The STIS has two Multi-Anode MicroChannel Array (MAMA) detectors. The FUV instrument, MAMA-FUV, operates in the 1150--1700 Å spectral range and has a 25.1 × 25.3 arcseconds field of view. Observations with this instrument were taken with the E140M echelle centered at 1425 Å. The second detector has a spectral range of 1600--3100 Å and a 25.1 × 25.4 arcsecond field of view. It is aptly named the MAMA-NUV as its spectral range applies to NUV wavelengths. Observations were taken with the E230H echelle centered at 2713 Å. Both detectors have a pixel format of 1024 × 1024 and a pixel size of 25 × 25 μm.

Of the eight target stars, all were observed with the MAMA-NUV and also three with the MAMA-FUV. Having such a wide wavelength range enables analysis of multiple features of interest such as Lyman α (1215.6700 Å), DI (1215.3430 Å), and C II (1335.7077 Å) in the FUV, and Mg II (2796.3543, 2803.5315 Å) and Fe II (2594.499, 2606.462 Å) in the NUV (Morton 1991, 2003).

Observational Parameters for Targets

Target Name	Dataset	Observation Date	Exposure Time (s)	Aperture (as)	Filters/ Gratings	Central Wavelength Å	S/N (Mg II)
GJ3323	ocyw01010	09-22-2016	1613	0.2X0.09	E230H	2713	4.02
	ocyw01020	09-22-2016	2966	0.2X0.2	E140M	1425	-
HD32147	ocyw02010	09-16-2016	1879	0.2X0.09	E230H	2713	18.75
	ocyw02020	09-16-2016	2961	0.2X0.2	E140M	1425	-
GJ3325	ocyw03010	02-08-2016	1613	0.2X0.09	E230H	2713	0.39
GJ190	ocyw04010	02-08-2016	1836	0.2X0.09	E230H	2713	3.99
GJ173	ocyw05010	09-22-2016	1829	0.2X0.09	E230H	2713	2.83
	ocyw05020	09-22-2016	2961	0.2X0.2	E140M	1425	-
GJ9163	ocyw06010	01-25-2016	1825	0.2X0.09	E230H	2713	2.45
HD30523	ocyw07010	02-19-2016	1879	0.2X0.09	E230H	2713	4.85
HD29980	ocyw08010	07-24-2016	1879	0.2X0.09	E230H	2713	8.6

Table 2.2: Table displaying observational data for the eight targets with their datasets and corresponding observational parameters. The signal to noise ratio (S/N) for the Mg II emission lines is listed for each target. Low S/N greatly impacted our ability to fit absorption features, sometimes making it impossible.

Where a standard grating reads out a given spectral range in a single long diffraction order, an echelle grating has a groove shape that enables multiple diffraction orders to be stacked perpendicular to the incoming light, allowing for high efficiency over a wide range of wavelengths. Figure 2.1 shows how the E230H echelle stacks raw data. As the emission lines used to study the ISM are few and widely spaced, the echelle grating is extremely useful in obtaining data that allows us to study nearby clouds.

Mg II (A≈24) and Fe II (A≈56) are heavy elements that do not succumb to severe thermal broadening compared to lighter elements (e.g. D I, A≈2). As such, the lines are relatively narrow and require high resolution to resolve different velocity components of the LISM, as is the case with our sight lines, most of which have at least two components. Because the elements are in the NUV, the high resolution E230H grating enables us to resolve these elements. The MAMA-NUV observed the eight sight lines between January 21, 2016 and September 22, 2016.

All targets and associated observational parameters are listed in Table 2.2. Three of our sight lines were observed using the MAMA-FUV instrument, which encompasses a wavelength range that includes numerous emission lines (e.g. D I, H I, S II, Si II, Si III, O I, C I, C II, C IV). These ions are integral in the study of the LISM because from them we can extract characteristics such as temperature, turbulent velocity, and ionization structure. Elements such as deuterium and hydrogen are already thermally broadened, so they can be modeled with medium resolution spectra. Utilizing the medium resolution grating (E140M) on this instrument allows us to maximize the signal to noise ratio of the data and extract as much information as possible from the features.

The synthesis of FUV and NUV data paints a more detailed picture of local clouds of ISM, enabling us to more accurately reconstruct cloud morphology.

However, the raw data must be converted into a format where we can interpret the emission features present in the spectra.

2.3 Data Processing

The MAMA detectors count photons in order to produce two-dimensional UV images. Figure 2.2 shows the raw data from target HD29980, with arrows pointing to the two emission lines of the Mg II doublet.

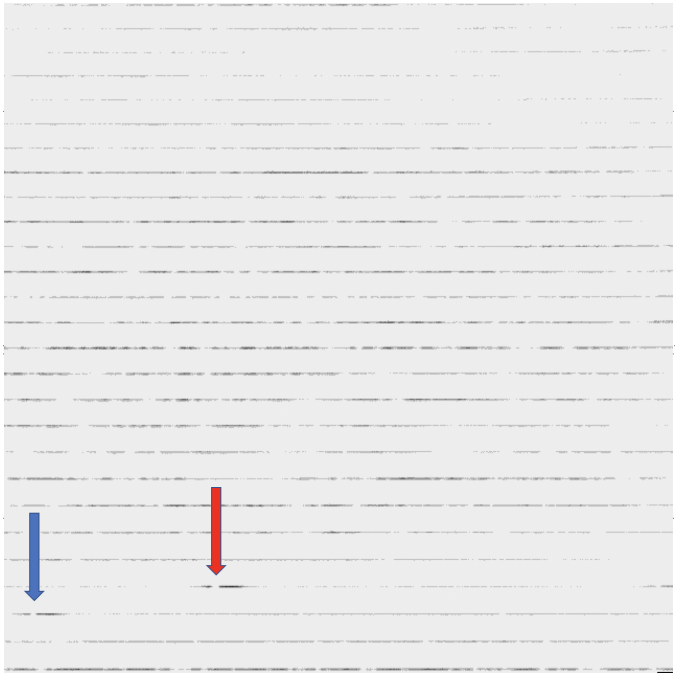

Figure 2.2: Raw data from the NUV-MAMA of target HD29980. Each dark line is an echelle order stacked vertically, and wavelength increases from left to right and top to bottom. A typical $\Delta\lambda$ for an echelle order is $\sim$14 Å. The arrows point out absorption from the LISM in the Mg II doublet at 2796 Å (red arrow), and 2803 Å (blue arrow).

Raw echelle spectral data obtained with STIS is processed through the `calstis` pipeline developed by the Space Telescope Science Institute (STScI) and improved using a two-dimensional background subtraction algorithm. The pipeline corrects for cosmic ray flux and performs basic two-dimensional image reduction (e.g.,

bias subtraction, dark subtraction, flat fielding)(Bostroem & Proffitt 2011). The pipeline performs a 1-D spectral extraction on the raw 2-D UV data, a function appropriate for point sources as in our observations. Extracting the spectrum produces a series of 1024 element arrays including flux, wavelength and error. The error array includes the propagated error for background noise. Each set of 1024 element arrays contain the wavelength range spanning a given echelle order ($\Delta\lambda \approx 14$ Å). The edges of each array have some overlap with the previous and subsequent one, which is an important consideration when fitting the data. Sometimes, part of an emission feature happens to coincide with the edge of an order and it is chopped off. Thankfully the size of the overlap is always wide enough to contain the entire emission line in the subsequent array, or we'd have to spend time reconstructing the emission profile. One can see in Figure 2.2 how close the blue arrow is to the edge of the echelle order.

Wavelength calibration is accomplished with two Pt-Cr/Ne line lamps which provide a reference spectrum in order to translate pixels on the detector into wavelengths.

Chapter 3

Fitting and Data Analysis

3.1 Flux Background

Many physical characteristics of the interstellar clouds can be extracted from the absorption profiles contained within a stellar spectra. Measurements such as radial velocity, column density, temperature, and turbulent velocity are crucial in reconstructing LISM morphology. To perform this analysis, we focus on the emission lines associated with elements that are abundant in the LISM (Redfield & Linsky 2008). At these specific wavelengths, we examine the stellar spectra for evidence of interstellar absorption. If absorption is present, we know a population of a given element is contained within the cloud.

However, we must first differentiate the absorption features from typical features in the spectra of the target star. To do so, we generate a continuum which is overlaid on top of the observed spectra of a given target star. In figure 3.1, the smooth, solid black line is the "flux background", our estimate of the stellar continuum free of any interstellar absorption. This fitting process has been employed effectively on numerous other ISM analyses (e.g. Redfield & Linsky (2008); Wyman & Redfield (2013); Malamut et al. (2014); Konow et al. (2020))

Mg II emissions (2796 Å and 2803 Å) from late type stars are characterized by a double peaked shape due to a temperature inversion in the stellar chromo-

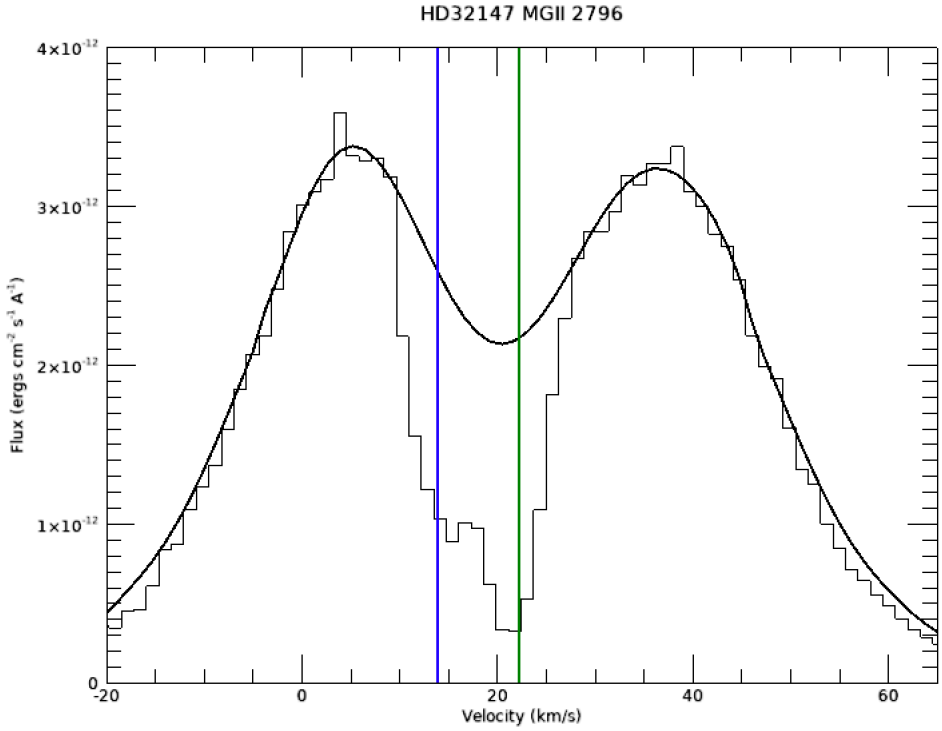

Figure 3.1: A plot of the Mg II emission line at 2796 Å. One can see the central reversal centered at ∼21.6 km s^{-1}, the radial velocity of HD23147. The green vertical line marks the ISM absorption with almost the same velocity as the star, and the blue line shows an absorption feature offset from the center. The thick black line is our estimate of the background flux without interstellar absorption.

sphere. We call the middle of this shape the "central reversal," a dip that aligns with the radial velocity of the target star (Genova et al. 1990). When interstellar absorption features are offset from the central dip in the stellar spectra, they are easier to distinguish. ISM absorption lines also tend to be much narrower than stellar features because they are not as thermally broadened as stellar atmospheres. However, this becomes trickier when the absorption features align with the center of the spectra, occuring when the radial velocity of the star matches that of a cloud of ISM. One can observe both cases in the Mg II spectra of Figure 3.1, where a deep absorption aligns with the central reversal (green vertical line),

and another is offset to the left at a lower velocity (blue vertical line). In this case, the significant depth at the center of the spectra gives us a clue that the central feature is not the result of a stellar contribution alone. But how can we solve this problem with a higher level of certainty? It is immensely helpful to view the data in a velocity space. Then, we can compare the known radial velocity of the star to the predicted velocity of the LISM absorption(s) along that line of sight (Redfield & Linsky 2008; Malamut et al. 2014; Konow et al. 2020). Looking at figure 3.1 again, we can see how the vertical blue and green lines, when set equal to the predicted radial velocity components of their LISM clouds, align with the absorption features in the spectra and help differentiate from intrinsic features of the stellar spectra.

For shorter wavelength emission features such as C II and O I, we do not fit for a double-peaked feature so a single peaked Gaussian is sufficient.

Once the absorption features are identified, we use `mkfb.pro` to fit the spectra as if absorption features are not present. In doing so, we have to fill in the gap left by interstellar absorption. Commonly, the easiest and most sufficient technique is a least-square polynomial fit ranging from integers 1-10. For the Fe II and Mg II fits, higher integers were required to fit more complex emission features (see Figures 3.2 and 3.4). When data was quite noisy (low signal to noise ratio), it was challenging to obtain a proper fit of the stellar spectra. The C II and O I emissions in Figure 3.5 were particularly difficult, as well as the Mg II emission in Figure 3.3. In these cases, the "click continuum" feature in `mkfb.pro` was employed. We place points along the path we expect the flux background to follow. Then the continuum is drawn when these points are connected.

3.2 Fitting ISM components

After the background flux has been produced, the fitting of absorption features can commence. We start with heaviest ions, Mg II and Fe II, because they have the strongest resonance lines. These ions produce narrow line widths and in turn more distinct ISM absorption features, providing the most accurate velocity measurements of clouds along the lines of sight. Fitting features associated with these ions first allows us to make more sense of how to fit absorption features at shorter wavelengths where the signal to noise ratio can be low (C II, O I). In our sample, Mg II proved to be the most useful in this task as only one sight line contained Fe II absorption features capable of fitting. In Figure 3.5, one can see how the Mg II lines have two distinct ISM features, highlighted by the blue and green dashed lines. The velocities determined from these fits were used as a basis for the analysis of the more poorly resolved Fe II, C II, and OI lines toward the same target.

ISM absorption features are fit with Voigt profiles, a convolution of a Lorentian and Gaussian profile which describe the shape of absorption caused by the ISM. These features are broadened by the turbulent velocity and temperature of interstellar clouds. Fitting the absorption features requires determining the number of components to fit the spectra with, as there can be multiple discrete clouds of LISM between us and the target star (Redfield & Linsky 2002). Each Voigt profile represents one discrete cloud in the LISM. The program `gismfit.pro` (written by S. Redfield and B. Wood, used in Redfield & Linsky (2002), Malamut et al. (2014), Zachary et al. (2018), Konow et al. (2020)) uses a number of inputs such as wavelength centroid, column density, and Doppler parameter which are varied to attain the minimum χ^2 value.

The Doppler parameter is related to the width of the absorption feature and is controlled by thermal broadening. Therefore, we can extract information about the temperature and turbulence within a cloud of LISM depending on the width of its absorption feature.

The column density is directly tied to the population of a given ion in the LISM. A higher column density means there is more material along a line of sight, inhibiting the amount of light that can reach the detector. If one were to point a laser through a dense fog, a detector on the other side would receive fewer photons from the beam compared to shooting it through a wispy, less dense haze. In figure 3.4, the left absorption feature (green dashed line) has a higher column density than the right feature (blue dashed line), causing a greater reduction in flux. Further a cooler, denser cloud would produce a narrower and deeper absorption feature because it would be less thermally broadened, and there would be more absorbing material between us and the target star. We would record a higher column density value and lower Doppler parameter from the cooler cloud.

Another input is the wavelength centroid which is the wavelength we expect to be at the center of the absorption component. This parameter is very important as it educates `gismfit.pro` where exactly it should judge the depth and width of this feature. Further, the wavelength input for the centroid is converted to the velocity corresponding to the cloud causing the absorption.

Because our targets are within a relatively close proximity to our solar system ($<\sim$50 pc), our fits required no more than a three components, most often requiring only two. We usually start with a single component fit, but for certain targets it is obvious that absorption features are caused by independent clouds (see Mg II k and h lines in Figure 3.5). However some spectra require further analysis because they have similar velocities, widths, and depths which does not

make it possible to easily distinguish from a one or two component fit (see Figure 3.2). In these cases, we employed the F-test to determine whether the one or two component fit is statistically justified.

In the F-test, we compare the reduced χ^2 value of the two fits, one being better (more model parameters, e.g. a two component fit) and one being worse (fewer model parameters, e.g. a one component fit). As we increase the number of components and in turn degrees of freedom to the fit, it becomes more complicated but does not mean the fit more accurately represents the actual number of components. If the fit with higher components passes the F-test, then it is statistically justified as the better fit and we consider adding more components. If it fails, the fit with one fewer component is what we proceed with.

An important characteristic of Mg II and Fe II is that they produce multiple resonance lines over a single wavelength range, allowing for two independent measures of the same, velocities, widths, and depths of absorption features along the same sight line. This is an advantage over fitting only one of the lines, as systematic errors resulting from the continuum fitting can be reduced by fitting the features simultaneously (Redfield & Linsky 2002). For one line, the fit parameters are frozen, forcing the components of the other resonance lines to have the same velocities, Doppler parameters, and column densities. If the fits are not consistent enough, the program refuses to run, often requiring a reconsideration of how we drew the stellar continuum. We completed simultaneous fits of the Mg II doublet for four targets seen Figures 3.2-3.5. These plots are labeled as Mg II k and Mg II k, showing the fits for the 2796 Å and 2803 Å lines respectively.

3.3 Error Analysis

After producing our first attempt at a best fit, we employ a Monte Carlo error analysis to determine the uncertainty of each parameter. A strength of Monte Carlo is its ability to highlight systematic errors rather than random error, so it is well suited to judge the precision of our fits. Monte Carlo generates between 0 and 100 random walks to judge which inputs adhere to the stated parameters of the `gismfit` model. The more random inputs we add, the more the uncertainty is improved. If our initial guesses are too far off, the program refuses to run and we must adjust our input parameters. The parameters and uncertainties of single ion fits, Fe II, C II, and O I, are determined by this method and listed in Table 3.2.

For the multiple resonance lines of Mg II, we can combine three different fits along the same sight line. We can simultaneously fit the Mg II doublet and combine the results of the Monte Carlo analysis with that of two single ion fits of the 2796 Å emission line and 2803Å emission line. The results of combining the parameters of each fit results in the weighted mean of the final values and their uncertainties. These are also listed in Table 3.2 for the Mg II ion of each sight line.

The final parameter values and their uncertainties seen in Tables 3.1, 3.2, and 3.3 are the weighted means of the parameters for the two individual fits and the simultaneous fit.

3.4 Fit Results

Of the eight sight lines observed, we were able to perform fits on four targets. Our greatest limitation was low S/N ratio. For each of the four analyzed, we performed simultaneous Mg II fits, obtaining an average of 2.25 absorption components along each sight line. For target HD32147, we were able to also fit one Fe II line (2600 Å), one C II line (1334 Å), and one O I line (1302 Å).

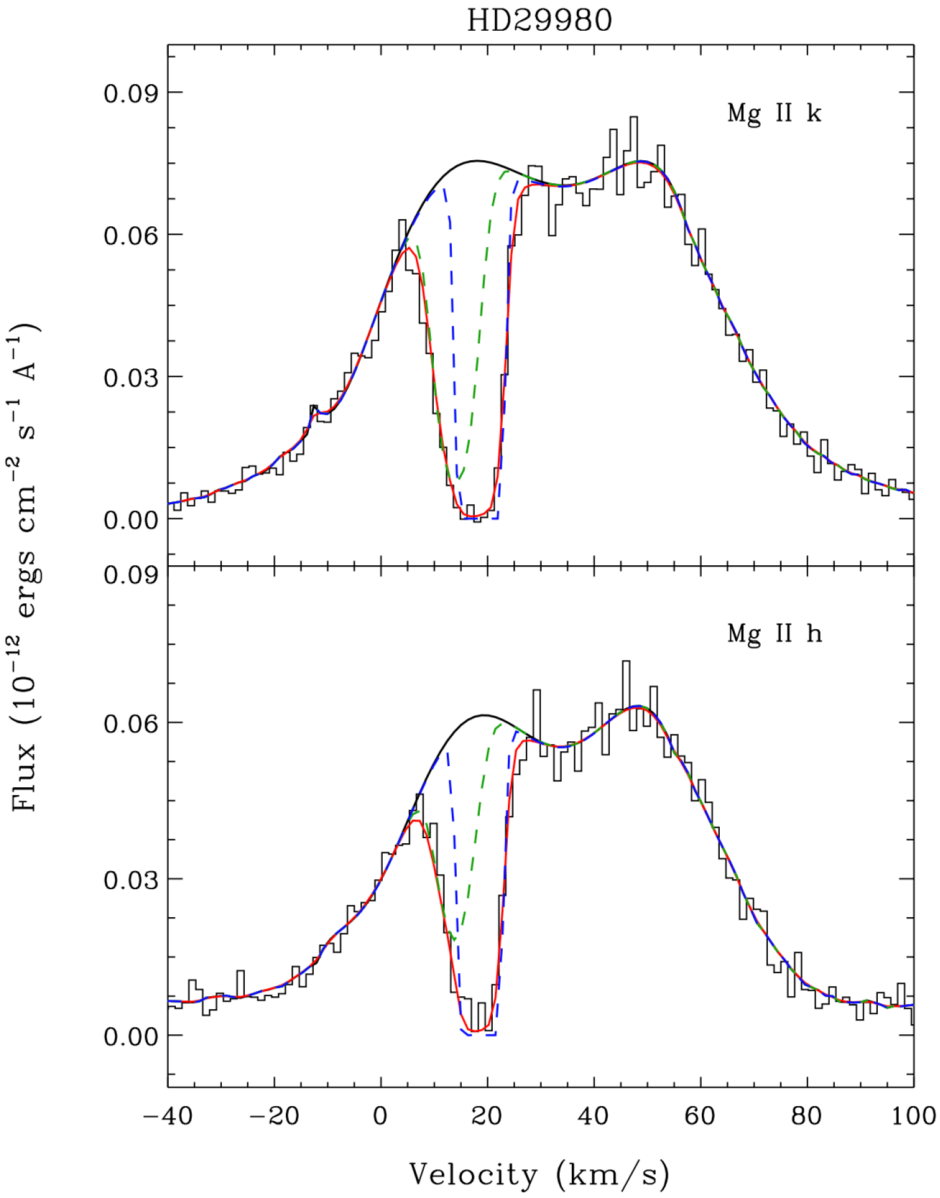

Figure 3.2: Best-fit result using our simultaneous fitting procedure on target HD29980 for the k and h Mg II resonance lines. There are two individual ISM absorption components, indicated by the blue and green dashed lines. They are fairly blended compared to other sight lines. The histogram is the observed flux data and the solid black line shows our estimate for the stellar continuum if no interstellar absorption was present. The red line is the total absorption of all components convolved with the instrumental line-spread function.

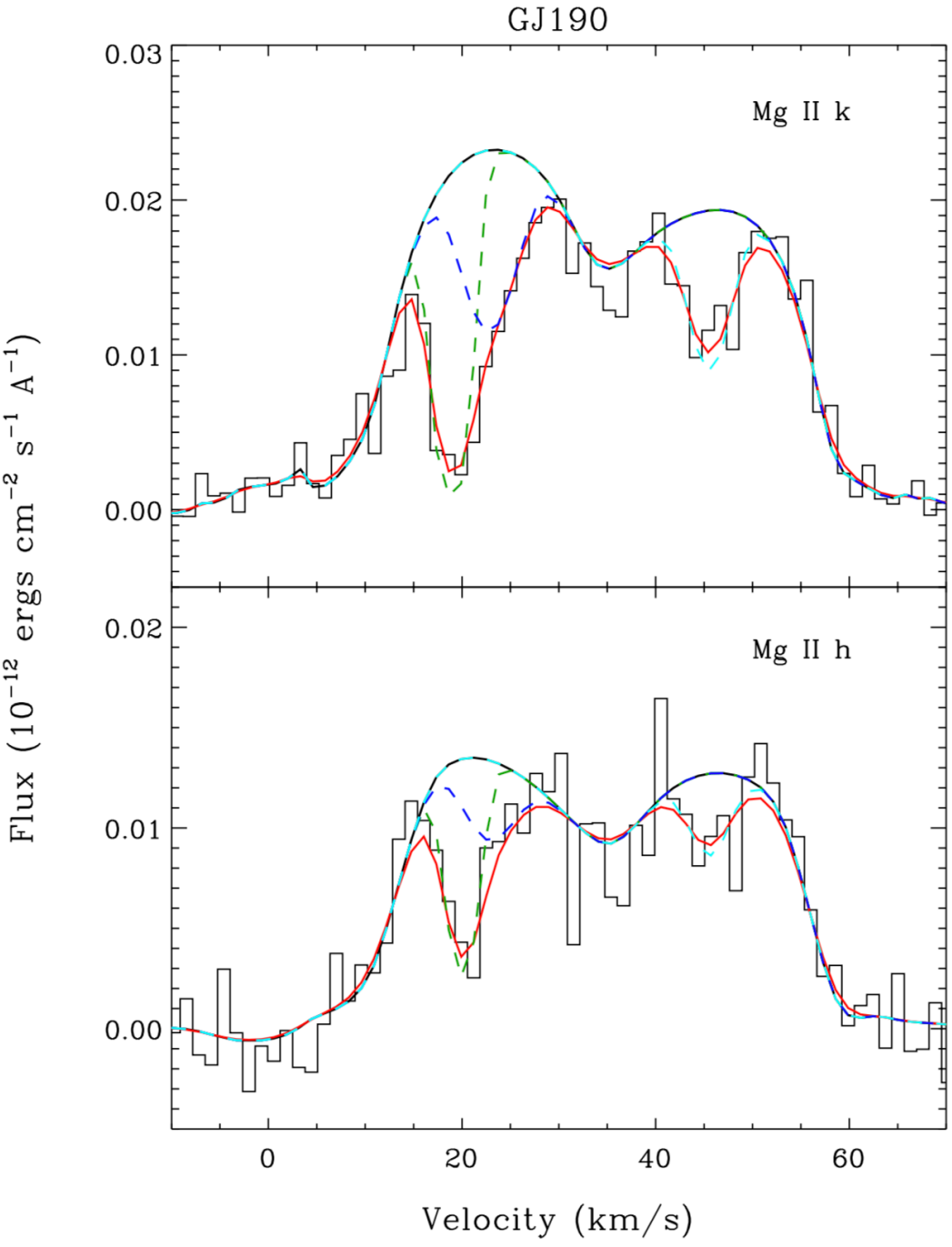

Figure 3.3: Same procedure as Figure 3.2 but for target GJ190. Notice a third absorption component at ∼45 km s^{-1}.

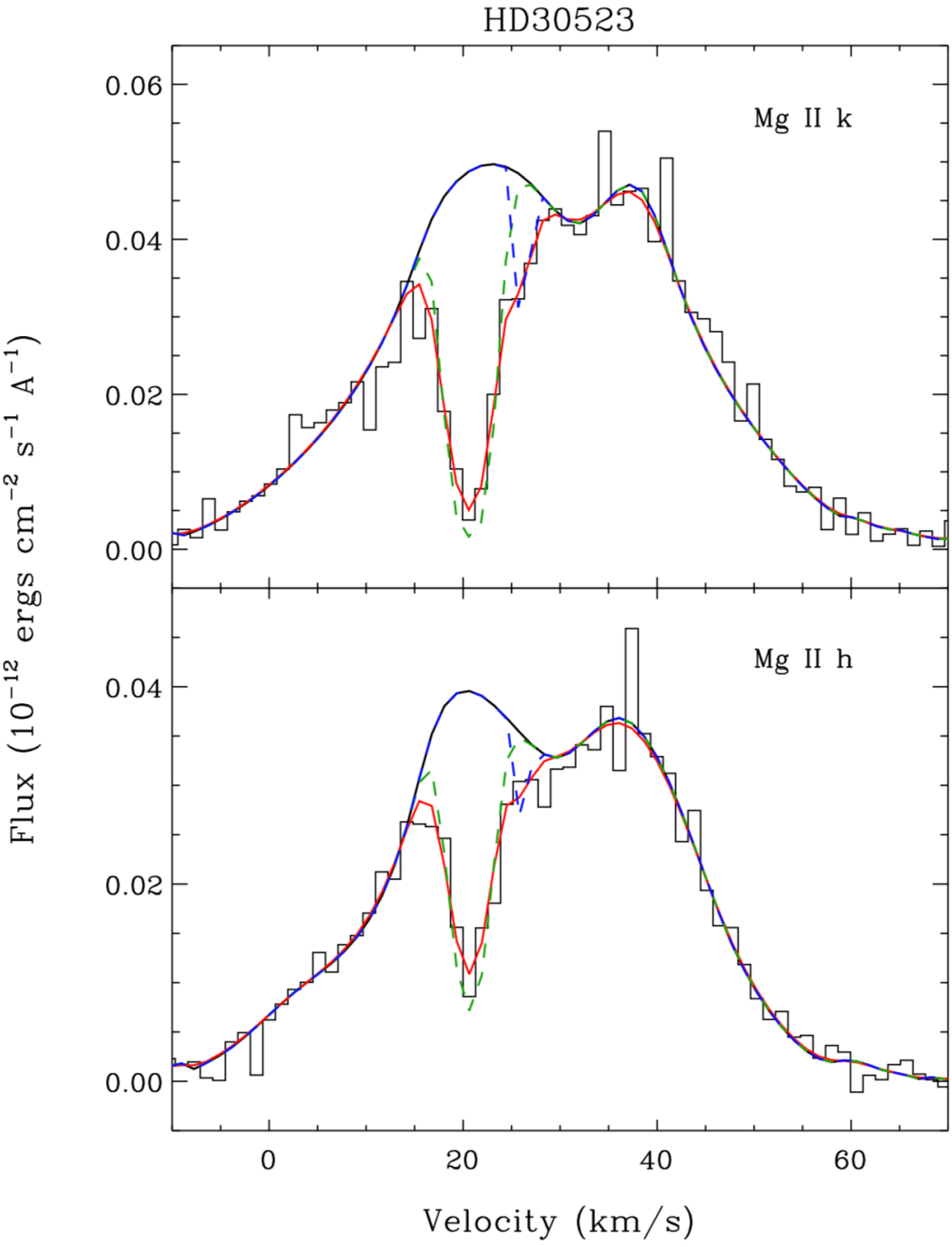

Figure 3.4: Same procedure as Figure 3.2 but for HD30523. We see one much weaker absorption feature compared to other targets.

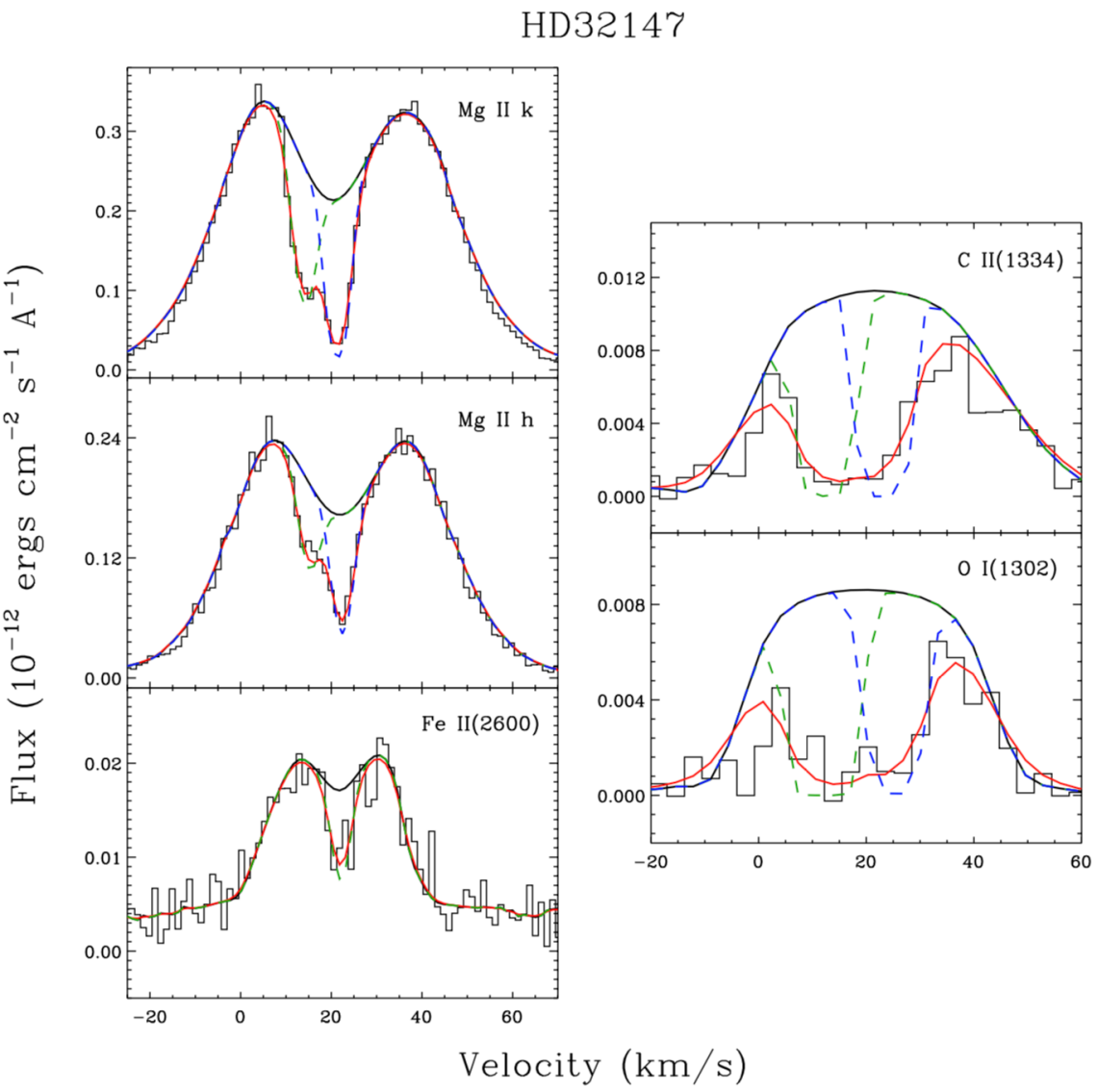

Figure 3.5: Same Mg II fitting procedure as Figure 3.2 but for HD32147. We were unable to perform a simultaneous fit on the Fe II doublet, but achieved a single component fit at the 2600 Å resonance line. One of the components present in the Mg II fit is not present, possibly implying a low abundance of Fe II ions compared to the other cloud. The C II and O I emission lines suffer from blending and a low signal to noise ratio, but we were able to extract a two component fit based on the velocities calculated the Mg II fit.

We will first talk about HD32147 and HD29980, as they had the most resolved components contained in the Mg II emission lines and were the most straightforward to fit. HD29980 (Figure 3.2) has ISM absorption that is clearly offset from the central reversal, making it easily distinguishable from stellar contributions. However, the blending of the features does not make it obvious a two component fit is required. The F-Test proved its value here as the two component fit was statistically justified when compared with the one component and two component fit. Further, the Doppler parameter of a single component fit was $\sim$6 km s^{-1}, significantly greater than the average b values of numerous sight lines analyzed in Redfield & Linsky (2004) which is $\sim$4 km s^{-1}.

Target HD32147 (Figure 3.5) offered the most straightforward fitting, as the two components were distinguishable visually. One absorber shares a similar velocity to the target star, but the depth of its feature differentiates it from the central reversal. The velocity components extracted from these fits provided a basis for the other more poorly resolved lines in the spectra of HD32147. C II and O I are far more saturated making it difficult or next to impossible to differentiate between the two features, so we can use the velocity values from the Mg II fits as our basis because they are on the same line of sight. Interestingly, the Fe II line has only one significant absorption feature that shares a similar velocity to that of the Mg II lines. This may indicate a significant difference in abundance of Fe II between the two clouds.

Throughout all of the targets, we see a trend of at least two components. The Mg II doublet is very important for this assessment because of the following: aside from the simultaneous fitting, we can visually compare the k and h lines to one another and identify absorption components that otherwise may go unseen. For instance, in Figure 3.4, the second (blue dashed line) absorption is not hard to

distinguish in the h line. But in the k line, one can see a subtle change in the slope of the absorption feature around 25 km s^{-1} where it slants to the right. Adding the blue component more accurately describes the spectra than a single component would.

Finally, in target GJ190 (Figure 3.3), we see a third absorption component at a much higher velocity compared to the other sight lines. Because it appears in both the h and k lines, we do not expect it is an anomalous artifact of the stellar continuum. We will discuss this further in Chapter 4.

3.5 Final Fit Parameters

In this section, we present the fit parameters resulting from the fitting. Table 3.2 presents the velocity (v), Doppler parameter (b), and column density ($\log N$) associated with the individual components of each of the four targets. Only for HD32147 were we able to fit emission lines other than magnesium. Most of the velocity values range from ∼14--25 km s^{-1}, but there are outliers. The third component of GJ190 has a velocity of ∼45km s^{-1} from an LISM cloud that is not present in any other sight line. The velocities produced by the C II and O I fits of HD32147 deviate from the Mg II results and suffer from a much greater uncertainty. We expect this is due to the blending of the C II and O I lines and will rely on the Mg II velocities when we discuss cloud identification.

The Doppler parameter, measured by the width of the absorption component, has an average value of $b \approx 3$ km s^{-1}. The third second component of HD30523 deviates furthest from this value with a measurement of 0.93 ± 0.79 km s^{-1}.

Table 3.2 Fitting Components

Target	Ion	Component Number	v km s^{-1}	b km s^{-1}	log N cm^{-2}
HD32147	Mg II	1	14.42 ± 0.31	3.04 ± 0.14	12.133 ± 0.0314
		2	21.77 ± 0.30	2.68 ± 0.14	12.437 ± 0.00265
	Fe II	1	22.13 ± 0.62	2.54 ± 1.00	12.372 ± 0.0933
	C II	1	11.34 ± 2.19	3.77 ± 1.17	14.125 ± 0.355
		2	23.12 ± 2.56	3.71 ± 2.059	14.211 ± 0.754
	O I	1	11.00 ± 3.729	4.19 ± 1.46	14.966 ± 0.356
		2	25.28 ± 2.09	4.29 ± 1.14	14.40 ± 0.295
GJ190	Mg II	1	19.77 ± 0.57	1.87 ± 0.36	12.425 ± 0.0541
		2	23.26 ± 1.21	3.17 ± 0.93	11.805 ± 0.215
		3	45.58 ± 0.34	2.80 ± 0.52	11.926 ± 0.0228
HD30523	Mg II	1	20.66 ± 0.13	2.32 ± 0.15	12.489 ± 0.00754
		2	25.90 ± 1.27	0.93 ± 0.79	11.331 ± 0.0700
HD29980	Mg II	1	14.06 ± 0.92	4.08 ± 0.83	12.576 ± 0.0344
		2	18.56 ± 0.75	2.18 ± 0.11	13.077 ± 0.698

Table 3.1: Table displaying data sets from the campaign and associated target stars, radial velocities, and near ISM clouds along the associated sight lines.

The log column densities have a range between ∼11 and 15 cm^{-2}. It is worth noting that the components experiencing the most blending skew this average, particularly those from the C II and O I fits of HD32147. Omitting these may give us a more realistic measurement of the average density of the clouds in our sample. Though HD29980 was also blended, we do not see as significant of errors in the fit components.

These parameters provide the basis for rebuilding the morphology of the LISM along the historical trajectory of the Sun's travel. In the following chapter, we will discuss the kinematic structure of these clouds and the effects it would have had on our solar system.

Chapter 4

Discussion

In this chapter, we discuss use the values attained from fitting to reconstruct the morphology of the nearest clouds of Local Interstellar Medium. Then we will combine this knowledge with the movement of both the clouds and Sun with respect to with one another to better understand the environment our solar system has traversed over the past ∼4--5 million years, and its relationship to the expansion or contraction of the heliosphere. Further, we will discuss on the astrospheric astrospheric detections for two targets.

4.1 Reconstructing Cloud Morphology

Here we present our discussion of the fit results from Chapter 3, starting with how we identify known clouds based on their velocity measurements. Once we tie a cloud to a velocity associated with a particular cloud, we use our column density measurements to estimate the distance to the edge of each cloud present along four sight lines. Tying distance measurements to specific clouds along the historical solar trajectory allows us to establish a timeline of interaction between the Sun and specific clouds in the LISM.

4.1.1 Cloud Identification

We previously listed the physical parameters from our fitting results, but now we will focus on the radial velocity measurements and discuss how well they compare to known LISM cloud velocity vectors. Based on a comprehensive database of 270 individual velocity components along 157 sight lines, Redfield & Linsky (2008) developed a LISM velocity prediction tool called the Kinematic Calculator. For a given set of coordinates, the calculator conveniently predicts the velocity of the of cloud(s) traversing, within 20°, or beyond 20° the corresponding line of sight. Malamut et al. (2014) confirmed the Kinematic calculator's accuracy by comparing it to velocity measurements along 34 sight lines. We use the calculator to discern which measured velocities agree with which clouds. Table 5.1 shows the predicted clouds and velocities corresponding to targets we were able to extract velocity measurements from.

A "cloud" refers to a discrete body in the LISM with homogeneous kinematical and physical properties. We also assume the clouds have sharp edges at their borders and that the flow and mixing of gas within is consistent throughout. There are 15 possible clouds that could traverse a line of sight, and the borders of the LIC are most well established because it appears in 79 sight lines of the sample of 157. Though individual clouds can be identified with far fewer observations, their borders are less well constrained and harder for the calculator to predict accurately. One example is the Aur cloud (9 observations) that has a thin structure, taking up less angular area on the sky (Redfield & Linsky 2008).

Predicted Clouds and Velocities for Targets

Target	Component Number	v_r (o) kms^{-1}	v_r (p) kms^{-1}	Cloud
HD32147	1	14.42 ± 0.31	13.83 ± 0.91	Blue
	2	21.77 ± 0.30	22.15 ± 0.99	LIC
GJ190	1	19.77 ± 0.57	19.76 ± 1.08	LIC
	2	23.26 ± 1.21	24.30 ± 0.88	Aur
	3	45.58 ± 0.34	$43.17 \pm 1.93,\ 52.03 \pm 1.76$	Vel, Cet?
HD30523	1	20.66 ± 0.13	22.16 ± 1.03	LIC
	2	25.90 ± 1.27	24.22 ± 0.89	Aur
HD29980	1	14.06 ± 0.92	13.36 ± 0.96	Blue
	2	18.56 ± 0.075	21.34 ± 1.02	LIC

Table 4.1: For each target, the component number corresponds to the same component number listed in Table 3.2. We compare the observed velocity to the predicted velocity to confirm the predicted cloud. v_r(o) and v_r (p) denote the observed and predicted velocity component respectively. The predicted cloud and velocity component are based on the Kinematic Calculator (Redfield & Linsky 2008).

The Kinematic Calculator estimates are in close agreement to the majority of our velocities. In each sight line, we see a velocity component we can identify as the LIC. The greatest deviation from the predicted LIC component is seen in HD29980, most likely due to blending of the interstellar absorption features. We are confident this is a positive identification of the LIC because it is observed in each target, predicted to traverse this line of sight, and no other predicted velocities provide a match better than the LIC. Further, our targets are in a downwind direction (or could say along historical trajectory), and in both all sky surveys by Redfield & Linsky (2008); Malamut et al. (2014) and Wyman & Redfield (2013)'s study of targets specifically in that direction, the LIC dominates that portion of the sky. In the LIC we see variations in column density even in small area of the sky our sight lines cover. This implies a complex small-scale structure and that the LIC is not a homogeneous clouds.

In two targets, HD32147 and HD29980, we identify velocity components of

the Blue cloud. This cloud is predicted to be within 20° of the sight line of both targets. Among the clouds that were within 20°, the only competing lower velocity cloud was Hyades, but it had an estimated velocity of ∼11 km s^{-1} for both targets, so it was not a strong match.

The Aur cloud is identified in the other two sight lines, GJ190 and HD30523. In HD30523, the Aur was within 20° and predicted velocity closely matched the observed velocity. Aur was harder to identify for GJ190 because it did not traverse nor was it $< 20°$ of the sight line, but its velocity (24.3 ± 0.88 km s^{-1}) most closely matched our observation. We did not consider the clouds within 20° to be contenders because their velocities were ∼10 to 15 km s^{-1} away from our measured velocity of 23.26 ± 1.21 km s^{-1}. Three other clouds with angular separation $> 20°$ had similar velocities to the observed value: G (24.98 km s^{-1}), Mic (24.34 km s^{-1}), Eri (22.03 km s^{-1}). However, the angular separations between the central coordinates of these clouds (Redfield & Linsky 2008) were 95°, 164.4°, and 121.2° respectively. Aur's separation is 41.5°, far less than the others. This is still a substantial separation from the historical trajectory, but because the cloud has a filamentary structure, it is prone to large error in the estimated boundaries (Redfield & Linsky 2008). Further, HD30523 is the closest ($\sim 8.8°$ separation) target to GJ190 we were able to fit, and its second velocity component matches Aur. Figure 5.1 shows an estimate of where the cloud borders exist based on our findings and those established in Redfield & Linsky (2008) and Linsky et al. (2019). It is worth noting that based on the detection of Aur toward target GJ190, it should be resized to ensure the target is within its borders.

Finally, GJ190's third component is unidentified at this point. The velocity of Vel closely matches the observed velocity of the mystery component, but is $> 60°$ from GJ190's path. The Cet cloud is a possible but less likely candidate because

of its high velocity, but again the angular separation is $\sim 60°$. Most likely, the borders of Vel are not constrained well enough to make a positive identification.

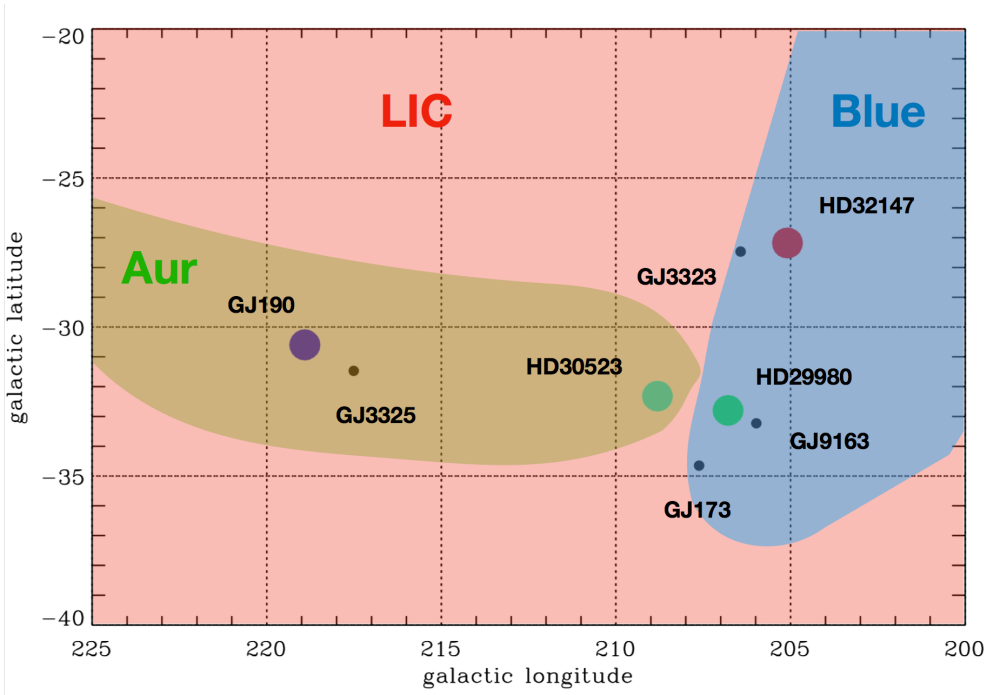

Figure 4.1: A plot in galactic coordinates of the target stars in our sample and the detected clouds. The colored, larger circles show the stars whose spectra we were able to fit. The LIC is present in every sight line and encompasses most of the sky, so it occupies the entire plot. The Aur cloud is seen in green, and within its borders are targets GJ190 and HD30523, both of which showed an ISM component from Aur and the LIC. The Blue cloud is represented by the blue space extending down from the upper right corner. Within its borders are HD32147 and HD29980, which both show ISM components from the LIC and Blue cloud.

Even in this 2-D display of a small area of the sky, the LISM has a diverse range of cloud shapes and velocities. In the next section, we will attempt to add another dimension by calculating the distances to the edges of these discrete clouds along the four lines of sight along which we were able to detect interstellar

absorption.

4.1.2 Distance to Cloud Edges

Determining the distance to the edges of clouds in the LISM is crucial. Not only is it key in reconstructing the general morphology of the clouds of LISM, but it also provides the basis by which we determine the time it takes for the Sun to traverse a given cloud and reconstruct the timeline of interstellar travel.

In order to make this calculation, we have to make a series of assumptions: we assume these clouds have constant neutral hydrogen density. By dividing the neutral hydrogen column density $N_{\rm HI}$ by the volume density $n_{\rm HI}$, the path length of the absorbing medium is then determined (Linsky et al. 2019). We take $n_{\rm HI}$ to equal 0.2 cm^{-3} based on in-situ helium measurements (Gloeckler et al. 2004) and He I/H I measurements from extreme-UV observations of local white dwarfs (Dupuis et al. 1995), and apply it to all three clouds. Redfield & Linsky (2000) compared the LIC and Hyades cloud and found that the column densities do not vary by more than a factor of two and both are well mixed. The rough homogeneity between two separate clouds of LISM support that this assumption is reasonable, though it is more likely the true density structures of individual clouds are more complex. Without in-situ measurements, this is our best guess at the volume densities of the clouds, and provides consistency between the border estimates. Additionally, we assume the clouds have sharp edges (Redfield & Linsky 2008).

Hydrogen column density is quite difficult to measure toward nearby stars because the Lyman-α emission is saturated, but because D I is a very reliable tracer of hydrogen within the Local Bubble, it provides us with the most reliable measure of distance. The D/H ratio $= 15.6 \pm 0.4 \times 10^{-6}$ (Linsky et al. 2006).

We also use Mg II and Fe II as they have tight correlations with H abundance, though they do suffer from depletion onto dust grains (Linsky et al. 2019). They are Mg II/H I = $3.6 \pm^{2.8}_{1.6} \times 10^{-6}$ and Fe II/H I = $2.14 \pm^{0.61}_{0.48} \times 10^{-6}$ respectively. Once we convert the column densities from our calculations, they can be input into the following equation to calculate the distance (d_{edge}) to cloud edge (Redfield & Linsky 2008; Linsky et al. 2019).

$$d_{edge} = \frac{N_{\rm HI}}{3.806 \times 10^{18}\ n_{\rm HI}}$$

We were able to calculate the borders of four targets, all with Mg II and one with D I. The results are listed in Table 4.2.

Cloud Edge Calculations

Target	Ion	LISM Cloud	d_{edge} pc
HD32147	Mg II	Blue	$0.50\pm^{0.39}_{022}$
	D I (1)	Blue	0.23 ± 0.28
	Mg II	LIC	$1.00\pm^{0.78}_{0.44}$
	D I (1)	LIC	0.69 ± 0.13
GJ190	Mg II	LIC	$0.97\pm^{0.77}_{0.45}$
	Mg II	Aur	$0.23\pm^{0.18}_{0.10}$
	Mg II	?	$0.31\pm^{0.24}_{0.14}$
HD30523	Mg II	LIC	$1.13\pm^{0.88}_{0.50}$
	Mg II	Aur	$0.078\pm^{0.062}_{0.037}$
HD29980	Mg II	Blue	$1.07\pm^{1.076}_{0.62}$
	Mg II	LIC	$4.39\pm^{7.80}_{7.29}$

Table 4.2: The table displays the target star, the cloud associated with that target, and the calculated distance to the cloud edge, d_{edge}. For each sight line, the ion corresponds to the emission feature from which the column density was measured. The column density is then used in the d_{edge} calculations (see body text for calculations). (1) The column densities used in this calculation were obtained via private communication with Brian E. Wood.

Because D I is the best tracer of hydrogen, we assume it is the most reliable

reliable measurement, followed by Fe II then Mg II. We also take into consideration that the lines with poor signal to noise ratio or blending of absorption features have higher uncertainty and are less reliable. The affects of blending are made clear with HD29980 LIC measurement, $4.39\pm^{7.80}_{7.29}$. We heavily favor the LIC d_{edge} measurements of the other targets because HD29980 deviates so greatly from the other distance calculations. HD32147 is the most reliable because it has the highest S/N, the components aren't blended, and we have D I measurements. The Blue cloud measurements have a median value of $\sim$0.50 pc. This is within the range of error on the D I measurement, but because D I is our best measure of H I density, we expect the Blue cloud edge is $<$0.5 pc. For the Aur cloud, we have the least amount of information, and rely solely on Mg II for d_{edge} calculations. Target HD30523 has a signal to noise ratio 0.86 greater than GJ190, but the Aur absorption component in HD30523 is much smaller and shallower compared to GJ190. The higher signal to noise may provide a more reliable measurement, but the discrepancy between edge distances could also be explained by a difference in the thickness of absorbing material. Figure 4.1 shows how close HD30523 is to the edge of the cloud. This edge region may be thinner than the region away from the edge where GJ190 resides.

For the LIC, we have the most information on the distance to its edge, as it occupies the majority of the sky. Though the errors of the Mg II measurements are significant, the median value is around 1.06 pc. However, again we lean more heavily on the D I measurement as it has the smallest error and most reliable measurement. Therefore, we expect the d_{edge} measurement is $<$ 1 pc.

The cloud edge measurements as a whole follow a trend: they are all smaller than the average cloud widths in the LISM (Redfield & Linsky 2008). This may be from the because the paths toward the stars in our sample only traverse border

regions of the cloud. In Figure 4.2, the contours of all clouds that we detect are plotted along with the paths toward our target stars, represented by various colored lines extending from the (0,0) coordinate toward the bottom left of the figure. None of the sight lines pass through the bulk of any of the three clouds and seem to only traverse the edges, which is why we may be obtaining shorter cloud edge distances in general.

The borders of the LIC are well constrained as analyses of numerous sight lines have produced a 3-D model of the LIC (Redfield & Linsky 2008; Linsky et al. 2019; Redfield & Linsky 2000). However, our sight lines present the best observations of the LIC along the historical trajectory of the Sun so the model can be improved for this area of the sky. For the Aur and Blue cloud, these measurements are even more important because there are far fewer detections of these clouds. Additional border calculations will improve the 3-D model of the LIC and educate future models of the Aur and Blue clouds. It is made clear in Section 4.2 just how important these measurements are in analyzing the history of the Sun's passage through the LISM.

4.1.3 Temperature and Turbulence

By obtaining the Doppler parameters from our data, we are capable of determining the contributions of thermal and turbulent broadening to the width of the absorption lines. We can use the following equation to relate the Doppler parameter (b) to the temperature (T) and turbulent velocity (ξ) of the absorbing gas:

$$b^2 = \frac{2kT}{m} + \xi^2 = 0.016629\frac{T}{A} + \xi^2$$

where k is Boltzmann's constant, m is the mass of the ion, and A is the atomic

weight of the ion in atomic mass units. To provide an accurate solution, the equation requires two ions vary greatly in mass. Two ideal candidates observed in the ISM are Iron and Hydrogen. As mentioned before, iron is a heavy element less prone to suffer from thermal broadening and has intrinsically narrow line widths. This helps us achieve a higher level of precision in both our calculations and differentiating between more than one absorption component (Redfield & Linsky 2004). If Fe II absoption isn't present, we can use Mg II as a less effective substitute because it is the next heaviest element we observe. Three of our targets were observed in the FUV wavelength range where the emission lines of the lighter elements are found. For one of our targets, HD32147, we have absorption in Mg II, Fe II, C II, O I, and D I. For the Fe II absorption, we only see one distinct absorption feature, but two the Mg II, so it may be the more sound choice for the calculation. D I provides a reliable measurement as it is less prone to saturation when observed over short sight lines, and it is the next lightest element after hydrogen (Redfield & Linsky 2004). Understanding the temperature and turbulence of clouds of LISM is critical in understanding the physical characteristics and environment associated with these clouds. In Figure 4.2 we present a visualization of the temperature and turbulent velocity calculated for HD32147. The temperature of the Blue cloud is $8870 \pm^{550}_{530}$ K and the turbulent velocity is $1.70 \pm^{0.35}_{0.41}$ km s^{-1}. The temperature of the LIC is $8990 \pm^{680}_{650}$ K and the turbulent velocity is $1.08 \pm^{0.56}_{1.08}$ km s^{-1}.

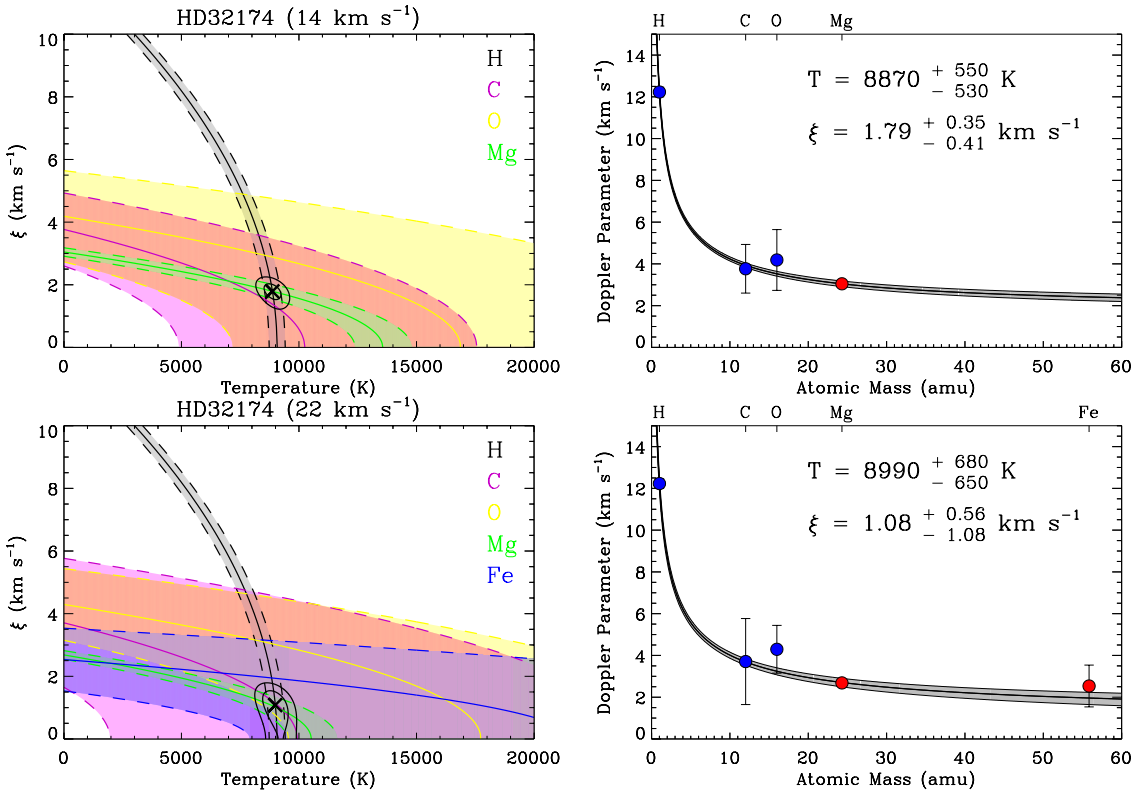

Figure 4.2: The left panels show a plot of temperature versus turbulence for a given ion, where the colors correspond to the ions listed in the upper right corner. The colored dashed lines are 1σ errors from the solid line which is from the equation listed previously. This results in a best fit curve in the plane of the graph. The black x is the best-fit value of the temperature and turbulent velocity (Redfield & Linsky 2004). The right two panels plot the Doppler parameter versus the atomic mass of the ions. Each dot is the value and error from our Doppler parameter calculations. The solid black line is a best fit for the temperature from the same equation. The top two panels are correspond to the Blue cloud absorption component, and the bottom two panels correspond to the LIC absorption.

4.2 Heliospheric Change With Time

Here, we present our analysis of the heliospheric response to its interstellar environment over the past ∼4--5 million years, the most recent timeline to date.

4.2.1 The Local Interstellar Environment

We will focus on the reconstruction of the past ∼150,000 years as most of the potential interaction with clouds of LISM seem to have occurred over this time. In order to accomplish this, we must first establish a frame of reference from which to view the LISM and solar motion. As shown in Figure 4.3, we chose to view from Galactic north, where the x-axis points to Galactic center and the y-axis points to Galactic east. The figure represents the configuration of the LIC, Blue, Aur, and Sun at present. At coordinate (0,0) black vertical and horizontal lines intersect to show the position of the Sun. Both axes are in pc so we can interpret the distance both the Sun and clouds move, lending a sense of scale and a basis for interpreting LISM-Sun interaction. Based on the previous section, we know that the LIC, Blue, and Aur clouds are along or close to the historical trajectory of the Sun, so these are the what we focus on as we look back in time.

After constructing a reference frame, we draw borders of the clouds. The LIC borders are by far the most robust because of the volume of data we have from the analysis of numerous sight lines containing LIC absorption and the consequent creation of a 3-D model (Redfield & Linsky 2008; Linsky et al. 2019). The LIC border shown in Figure 4.3 and 4.4 is a contour that lies flat on the Galactic plane, 0 pc above and 0 pc below. This is the same contour drawn in Linsky et al. (2019), and provides the most up to date model of the LIC. The outlines of the Blue and Aur clouds are based on the contours drawn in Frisch et al. (2011), but we adopt a tighter cloud configuration. Though one could vary these configurations to some degree because we are not sure of the distance between clouds along the same line of sight, we educate our model with which clouds appear in our sight lines. In order to be consistent with our observations, it required both the Blue and Aur

cloud to be moved closer to the LIC while maintaining a similar same shape. An alternative would have been to extend the cloud borders to encompass the sight lines, but that would have required moving cloud borders a considerable distance which did not seem as reasonable of an assumption.

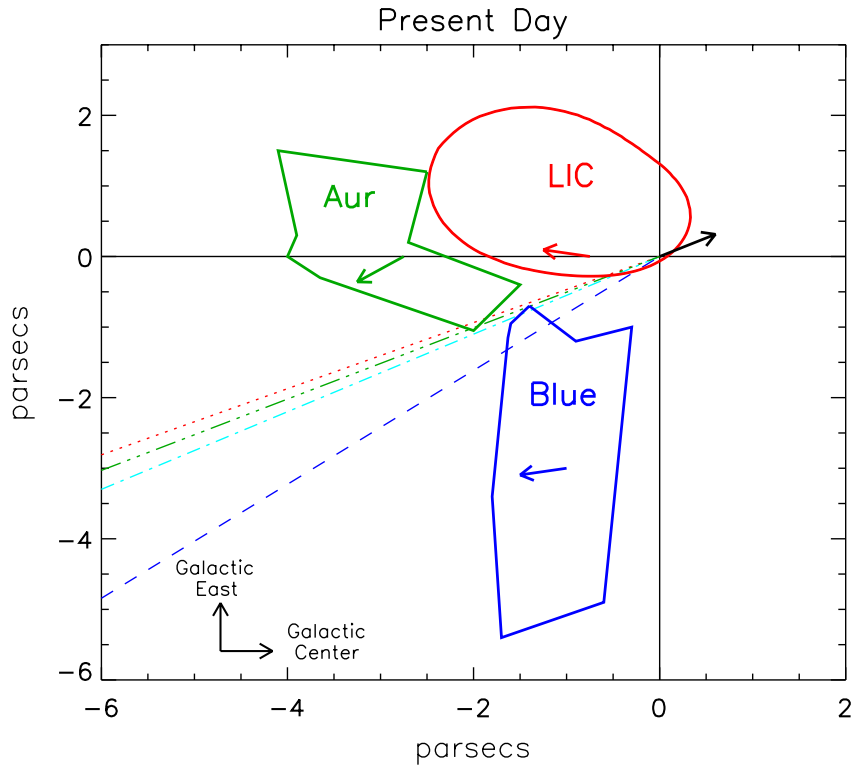

Figure 4.3: View from the north Galactic pole shows the configuration of the LIC, Aur, and Blue cloud at present. (0,0) marks the position of the Sun today. The colored arrows correspond to the direction of the flow vector within each cloud, and the black arrow corresponds to the direction of solar motion based on Dehnen & Binney (1998). All of these velocities are in the local standard of rest. The dashed lines show the path toward the four targets whose spectra we were able to analyze. Red dotted line: HD32147, green dashed line: HD29980, cyan dashed line: GJ30523, blue dashed line: GJ190.

We observed absorption of LISM between us and our furthest target star (50 pc). At its current velocity of 13.38 km s^{-1} in the local standard of rest (Schönrich et al. 2010), the Sun would have traversed this distance in $\approx$ 3.7 Myr.

With the cloud edges drawn, we could work towards getting the clouds moving.

Each arrow in Figure 4.3 is representative of a different velocity vector projected onto the Galactic plane. Their main purpose is to show the direction the Sun and clouds are moving toward. In general, the LISM clouds move with a bulk velocity in the same general direction, one that is almost perpendicular to solar motion (Frisch et al. 2011). Because we're going to be looking at past travel, the clouds and Sun will move in the opposite direction of the arrows shown in Figure 4.3. The red arrow pertains to the LIC, the green arrow to the Aur cloud, the blue arrow to the Blue cloud, and the black arrow to the Sun. U, V, and W are used to identify the magnitude and direction of velocity vectors toward Galactic center, Galactic east, and Galactic north respectively. This is convenient because in our chosen reference frame, U corresponds to the x-axis and V corresponds to the y-axis. We base the movement and trajectory of the Sun from Dehnen & Binney (1998) who calculated the Sun's velocity (km s^{-1}) in the Local Standard of Rest (LSR) to be $(U, V, W) = (10 \pm 0.36, 5.25 \pm 0.62, 7.17 \pm 0.38)$ based on the analysis of over 10,000 stars in the Hipparcos catalogue. We obtained heliocentric cloud velocities (km s^{-1}) from Redfield & Linsky (2008) for the LIC (23.84 ± 0.90), Aur (25.22 ± 0.81), and Blue (13.89 ± 0.89). We converted them to Cartesian coordinates (U, V, W) and subtracted the solar motion to get their velocities in the LSR. These velocities, along with the Sun's, are listed in Table 4.3.

Solar and Cloud Velocities in LSR

Moving Body	U (km s^{-1})	V (km s^{-1})	W (km s^{-1})
Sun (1)	10±0.36	5.25±0.62	10±0.36
LIC	-13.01	2.43	-12.74
Blue	-1.646	-0.305	-12.305
Aur	-10.52	-7.57	-14.29

Table 4.3: The LIC, Blue, and Aur velocities are in the Local Standard of Rest, derived based off of heliocentric cloud velocities from Redfield & Linsky (2008). These velocities are in Cartesian coordinates where U is toward Galactic center, V is toward Galactic east, and W is toward Galactic north. In Figures 4.3 and 4.4, we treat U and V as the x-axis and y-axis respectively, and use these velocities to calculate the movement of the Sun and clouds over time. (1) From Dehnen & Binney (1998).

Finally, we take the velocity measurements in the LSR for the Sun and clouds and project them across the U-V plane. We assume the clouds move as a whole with the same velocity over time. Figure 4.4 shows a series of panels tracking both the Sun's movement and those of the clouds in 20,000 year increments over the past 140,000 years. Each panel is labeled with a letter that I will refer to when discussing the timeline. Over the course of this time the Sun moved through the U-V plane a distance of 1.61 pc, and the LIC, Blue, and Aur cloud moved a total of 1.9 pc, 0.24 pc, and 1.85 pc respectively.

Approximately 140,000 years ago (panel g), the Sun transitioned from the hot, low density Local Bubble material and entered a denser area characterized by the warm, partially ionized gas of the LISM. Because the Aur and Blue cloud borders are not well constrained (Redfield & Linsky 2008), we can't be as definitive about which of the two clouds were traversed, but Figure 4.4 shows the Sun most likely experienced dynamical interaction with at least one cloud before entering the LIC. In its entry into LISM clouds 140,000 years ago, the Sun traversed the edge of the Blue cloud (panel g). This passage lasted ∼20,000 years before the Sun reentered the hot Local Bubble material (panel f). Then, the Sun passed close

to or traversed the Aur cloud ∼95,000 years ago (panel e). The Sun reentered the low density region around 85,000 years ago and traveled through it for the next ∼25,000 years before approaching the border of the LIC (panel d). Then approximately 50,000--60,000 years before present, the Sun traversed the LIC boundary (panel c) and enetered the region through which it has been traveling ever since. Our estimate for the LIC is close to the ∼47,000 year mean cloud crossing time stated in Frisch et al. (2011) for a constant cloud density of 0.2 cm^{-3} which is encouraging. However, because we analyze cloud passage along a very specific trajectory and incorporate the movement of the LIC independent of the Sun, we can say with more confidence that our timeline of 50,000--60,000 years is more definitive.

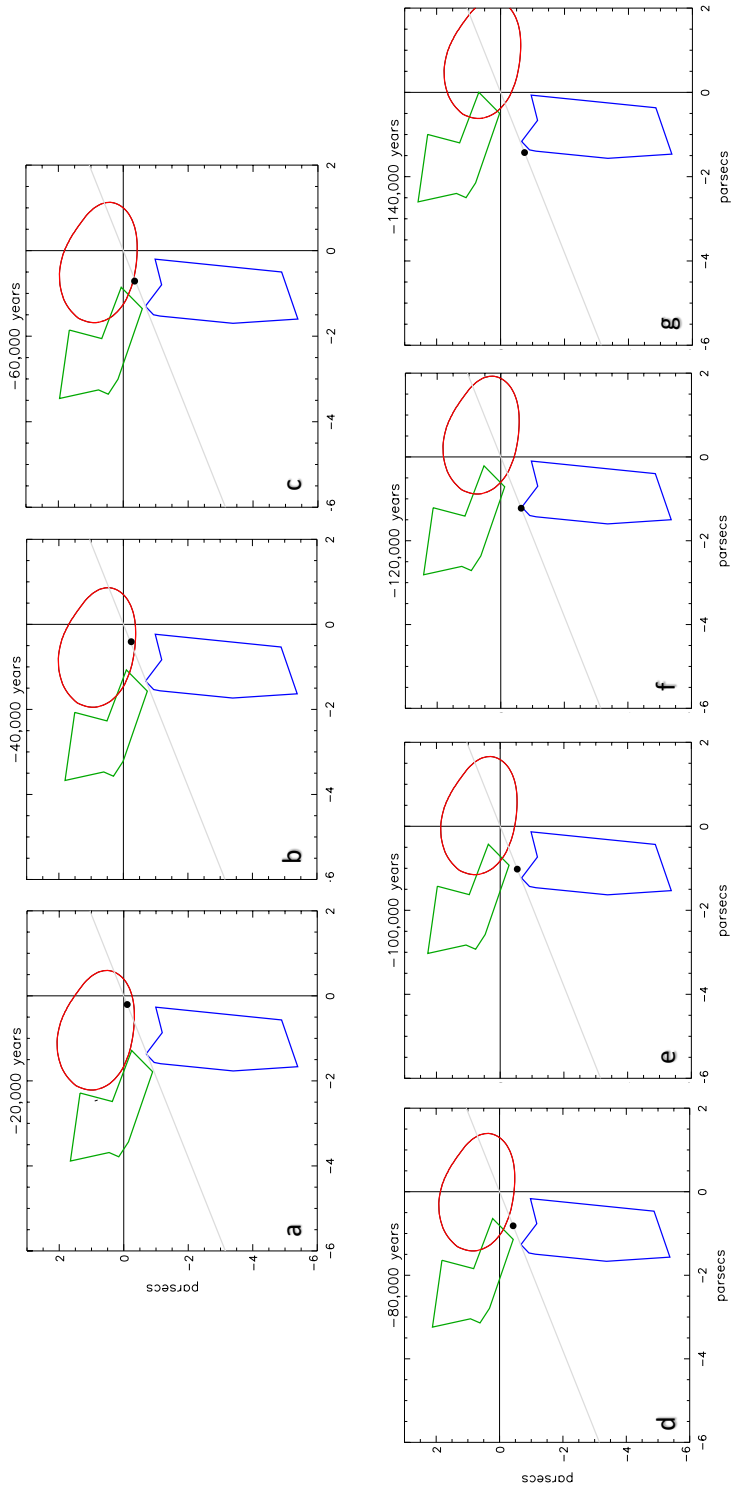

Figure 4.4: Viewing from Galactic north, we watch the Sun and cloud movement moving back in time over the past 140,000 years. The clouds are the same as in Figure 4.3, and move with a constant velocity opposite of the direction they travel today so opposite of the arrows in Figure 4.3. Starting with the upper left panel we move left to right, top to bottom, each panel jumping another 20,000 years into the past. The intersecting lines at (0,0) mark the Sun's position today. The black dot represents the Sun, and the light grey line shows the path of solar travel.

With the goal of improving our analysis in the future, we have to acknowledge that the reference frame puts a perspective bias on the analysis because we do not observe any movement toward or away from Galactic north (W-direction). Thus, the entry/exit timeline is not as accurate as it could be. However, we know that the LIC extends 2.4 pc below our contour line and 1.4 pc above it (Linsky et al. 2019), so we can more confidently say that our estimate predicts a realistic timeline for when the Sun entered into the LIC. Evaluating the trajectory of the Sun and LISM clouds from multiple angles will allow us to more effectively estimate the timeline of entry/exit from clouds.

The placement of the clouds also impacts whether or not the Sun actually traversed the Aur cloud or Blue cloud. We use a cloud configuration that packs them in tightly but in reality, we aren't sure of the space between the clouds because we don't have an estimate of cloud the volume density other than for the LIC (Frisch et al. 2011). The closest stars whose sight lines a given cloud traverses gives an upper limit for the cloud edge (Redfield & Linsky 2008), but this still may not provide enough of a constraint on cloud borders to say with certainty whether the Sun passed through it or not. If the clouds were farther apart, the Sun would have been less likely to traverse either of them. Further, if we were to change the assumed constant density of the clouds either higher or lower, the cloud borders would contract or expand in their current configuration, changing the timeline of passage in and out of the clouds.

While we acknowledge these uncertainties, our placement of the LIC, Aur, and Blue clouds is the best representation of our current understanding of the LISM. The assumed configuration is based on the results of the analysis of numerous sight lines through local interstellar material (Redfield & Linsky 2008; Frisch et al. 2011), and though we assume consistent density between clouds in order to draw

our cloud edges, the density we use is supported by multiple diverse measurements mentioned in section 4.1.2 (Gloeckler et al. 2004; Dupuis et al. 1995; Linsky et al. 2019). Based on our results, it is highly likely the Sun passed in and out of regions of varying densities over the past 140,000 years.

4.2.2 Heliospheric Response

With the timeline of cloud passage established in Section 4.2.1, we can now discuss the direct response of the heliosphere as the Sun passed through the varying conditions of the LISM. Our most basic assumption is that the density of each cloud clouds is the same, but our data tells us exactly when and where the contraction or expansion would occur. Muller et al. (2006) used the techniques developed by Zank et al. (1996) to model the varying environments our Sun could have experienced in its travel through the Milky Way. Even between us and nearby stars, the inhomogeneous LISM displays a wide range of distinct velocity components (Redfield & Linsky 2008).

To successfully model the interaction between the ISM and the heliosphere, a global heliospheric multifluid code is utilized. When interstellar neutrals travel inward through the heliosphere and interact with the plasma generated by the solar wind, a charge exchange occurs, throwing the neutral components out of equilibrium. The "multifluid" nature of the model manifests itself through considering four different fluids, three of which represent thermodynamically distinct plasma regions contained within the structure of heliosphere (see figure 1.5 in intro for structure). Neutrals vary depending the region they interact with. The fourth fluid region represents the protons of the plasma in the solar wind, as well as those of the interstellar plasma. (Muller et al. 2006; Müller et al. 2009).

The focus on neutrals allows for the model to effectively evaluation a wide range of interstellar environments. The hypothetical travels of the Sun take it through ISM with Densities vary 0.0005 to 15 cm^{-3}, up to 100 % ionization, and relative Sun-cloud velocities of up to 100 km s^{-1}. The model also assumes the Sun's output of solar wind is consistent. To model the solar wind at 1 AU, the parameters are 5.0 cm^{-3} for the plasma density (ρ_1), a temperature of 10^5 K , and a 400 km s^{-1} radial velocity (v_{SW}). Neutral hydrogen's gravity is assumed to balance radiation pressure and interstellar/heliospheric magnetic fields are ignored to simplify.

Based on the models of Muller et al. (2006), a relation was obtained that links the solar wind ram pressure $P_1 = \rho_1 v_{SW}^2$ at 1 AU and heliocentric distance to the total interstellar pressure P_{ISM}. The velocity of the the ISM (v_{ISM}) in the models is heliocentric. This results in the following equation for the radial distance of the heliopause from the Sun:

$$r_{HP} = r_0 \sqrt{\frac{\rho_1 v_{SW}^2}{P_{ISM}}} \left(1 - \frac{v_{ISM}^2}{v_{SW}^2}\right)^{\frac{5}{4}} \tag{4.1}$$

The constant r_0 is the result of theoretical heliospheric calculations and the fact that neutral hydrogen does not have major contributions to the pressure balance as it only weakly couples with plasma through charge exchange (Müller et al. 2009). r_0 is equal to 1.4.

A further outcome of the modeling of Muller et al. (2006) was a direct correlation between the heliopause and both the termination and bow shock. The entire system is in pressure balance, so the relation is linear.

$$r_{HP} = (1.40 \pm 0.03) r_{TS}$$

$$r_{BS} = (1.90 \pm 0.05) r_{HP}$$

From now on, I will call the bowshock BS, heliopause HP, and termination shock TS. Based on our analysis of the solar system's travel over the past ∼4 million years, the two major ISM environments we need to consider are the hot Local Bubble material and the warm, partially ionized gas of the local clouds. The Local Bubble is hot and almost completely ionized in its interior. Muller et al. (2006) adopt parameters suited to model this low density area ($n_{\mathrm{H\,I}} = 0.0005$ cm^{-3}, proton density = 0cm^{-3}, $v = 13.4$ km s^{-1}, $T_{LISM} = 1.26 \times 10^6$ K from Snowden et al. (1997)). The resulting boundaries place the TS at 90 AU and HP at 300 AU. There is no bowshock because the speed of sound in this plasma is 190 km s^{-1}, so the Sun is moving subsonically through the materialMuller et al. (2006).

To describe the contemporary ISM, they use parameters $n_{\mathrm{H\,I}} = 0.216$ cm^{-3}, $v = 26$ km s^{-1}, and $T = 7000$ K. These describe the temperature and velocity of the LIC, Aur, and Blue fairly well based on the values from Redfield & Linsky (2008). The volume density is also close to what we use for our cloud edge calculations (0.2 cm^{-3}). The contemporary heliospheric boundaries are thus TS=99 AU, HP=148 AU, and BS=285 AU.

The synthesis of our interstellar timeline and heliospheric models can now be accomplished. Between ∼4 million years and 140,000 years before present, the Sun traveled through the hot, low density Local Bubble material. We can make this assertion because the sight lines along the historical trajectory extend at most 50.5 pc, which doesn't go beyond the edge of the Local Bubble (Lallement et al. 2003). Thus, for a ∼3.86 million year period of time, the heliosphere was stable,

and the HP was 300 AU from the Sun, approximately twice the distance from where it exists today.

Then 140,000 years prior to present day, the Sun could have experienced a few different scenarios of cloud passage, but we will focus on two: either the Sun traversed no clouds but the LIC, or the Sun traversed all clouds. The former scenario is simple, as we can extend the timeline of maximum heliospheric expansion by between 80,000 and 90,000 years. If this were the case, the heliosphere would have been stable for 3.94--3.95 Mry before entering the LIC, where the HP was significantly compressed to 148 AU, *half* of the distance it was located through the vast majority of that time. From 50,000-60,000 years to present the heliosphere has remained relatively constant with the HP$\approx$ 148 AU.

In the case of the Sun traversing each cloud, there would have been multiple fluctuations in heliospheric boundaries over the past 140,000 years. The clouds are assumed to have consistent density throughout, so any encounter with a cloud, whether it be the middle or edge would have the same effect on the expansion/contraction of the heliosphere. 140,000 years ago, the Sun would have encountered with the Blue cloud, compressing the heliosphere during its 20,000 year passage. The Sun would then reenter the Local Bubble material 120,000 years from present day, and the heliosphere would once again expand and remain stable for $\sim$ 25,000. Then the Sun would contact the Aur cloud and the heliosphere would spend about 10,000 years compressed. Exit from the Aur places the timeline at 85,000 years from present. Next, the Sun would spend the $\sim$25,000 years back in Local Bubble material before approaching the border of the LIC. Finally, 50,000--60,000 years from present day, the Sun entered the LIC and the heliosphere was compressed, and the boundary conditions were pushed back toward the Sun where they have remained to this day.

As mentioned at the end of Section 4.2.1, changing the densities of the clouds to expand or contract would change the timeline we've constructed, in turn changing heliospheric response to the interstellar environment. If the clouds were far less dense than what we assume, the LISM could inhabit most of the space the Sun traversed and the heliosphere would have experienced compression less than at present but over a long period of time. Conversely, high-density clouds would occupy less space, but any interaction with clouds (though less likely) would cause a significant heliospheric compression.

4.2.3 Historical Implications on Earth

Muller et al. (2006) model the Galactic cosmic ray (GCR) transport for three different interstellar environments: hot Local Bubble void, the contemporary ISM, and a cool, neutral, dense cloud of ISM. Cosmic ray modulation across different heliospheric boundaries is primarily affected by the the size of the heliosphere and the environment inside the termination shock. Based on our analysis, the Sun encountered two environments described by their models, the hot Local Bubble material and the contemporary ISM. In both of these cases the heliosphere would not have experienced significant compression, so the influx of GCR in the Earth's atmosphere would not have changed to any great degree compared to current levels. Therefore, it is improbable the Earth's climate would have experienced significant change, or experienced higher levels of radiation.

Though the most recent interstellar environment did not prove to be dense enough to impact the inner solar system or Earth, the implications of a high density interstellar environment are still worth considering. Wyman & Redfield (2013) concluded that about 9-12 million years ago, the Sun passed through a high

density region that could have compressed the heliosphere to 21 AU, pushing the termination shock within the orbits of Neptune and possibly Uranus. During this time period, the planets would have been exposed to a high quantity of neutral ISM particles that characterize the hydrogen wall, as well as crossed into a region of of shocked LISM material. This time period is astronomically tiny, and with the diversity ISM in the galaxy one can only expect that during the Sun's life it will encounter numerous dynamic interstellar environments that could drastically alter the heliospheric boundaries.

4.3 Astrospheres

Just as our Sun's solar wind carves out a region in the surrounding ISM to form the heliosphere, so does the solar wind of other stars, forming "astrospheres," the heliospheric analogue for other star systems. Because the stellar wind produced by solar-like stars is relatively weak and fully ionized, direct detection is exceedingly difficult. Studying astrospheres gives us the ability to circumvent this problem, as they are a direct byproduct of stellar wind (Wood 2004).

When the stellar wind from solar-like stars and ISM interact, a charge exchange heats the population of hydrogen existing in astrospheres and creates a buildup of H I, forming a hydrogen wall. This accumulation of H I creates a broad, deep absorption feature at the Lyman-α line occurring at 1215.67 Å. However, the line is often highly saturated by H I from interstellar absorption, making it difficult to pick out the astrospheric signatures. In fact, for much of the past it was thought that the absorption seen at the Lyman-α line was due to solely interstellar H I, but this interpretation changed as more spectroscopic data of target stars was studied. In Linsky & Wood (1996)'s analysis of the sight line toward α-Cen,

there was a discrepancy between the Doppler parameter and heliocentric velocity extracted from the fit of the Lyman-α D I line versus the Lyman-α H I line. The H I Doppler parameter implied the cloud of ISM surrounding α-Cen was at a much higher temperature, and the velocity was redshifted 2.2 km s^{-}1 from where it should have been. They concluded that there was a parameter unaccounted for by the fit of the ISM absorption alone, but the cause was initially a mystery.

The solution soon arose from employing the same analytical techniques on sight lines to ϵ Ind and λ And (Wood et al. 1996) in addition to extensive heliospheric modeling (Gayley et al. 1997) that showed H I absorption from both our Sun's heliosphere and astrospheres was responsible. Further, the modeling showed that heliospheric Lyα absorption from the only accounts for the redshifted side of the Lyα line, and astrospheric absorption accounts only for the blueshifted side. Figure 4.5 illustrates this very well. The middle four panels show the path of the star's Lyα emission as it encounters different obstacles on its way toward our detectors. First, it encounters the hydrogen wall of its star's astrosphere, removing the middle of the line. Then, it traverses the interstellar environment, resulting in further absorption. Finally, it traverses the heliosphere, causing absorption on the redshifted side (Wood 2004). The lower panel shows the Ly α profile of α Cen-B. The black line is the stellar emission with no absorption and the dashed line shows the fit with ISM absorption alone. The green shading represents the absorption from the heliosphere and the red shading shows absorption due to an astrospheric component. The features present in this spectra cannot be explained by ISM absorption alone (Linsky & Wood 1996; Wood 2004).

The effectiveness of this method was used in further studies (i.e. Wood et al. (2001); Wood (2004)), substantiating the power of the Ly α H I line in the detection of astrospheres. It is also worth noting that analyzing heavier elements

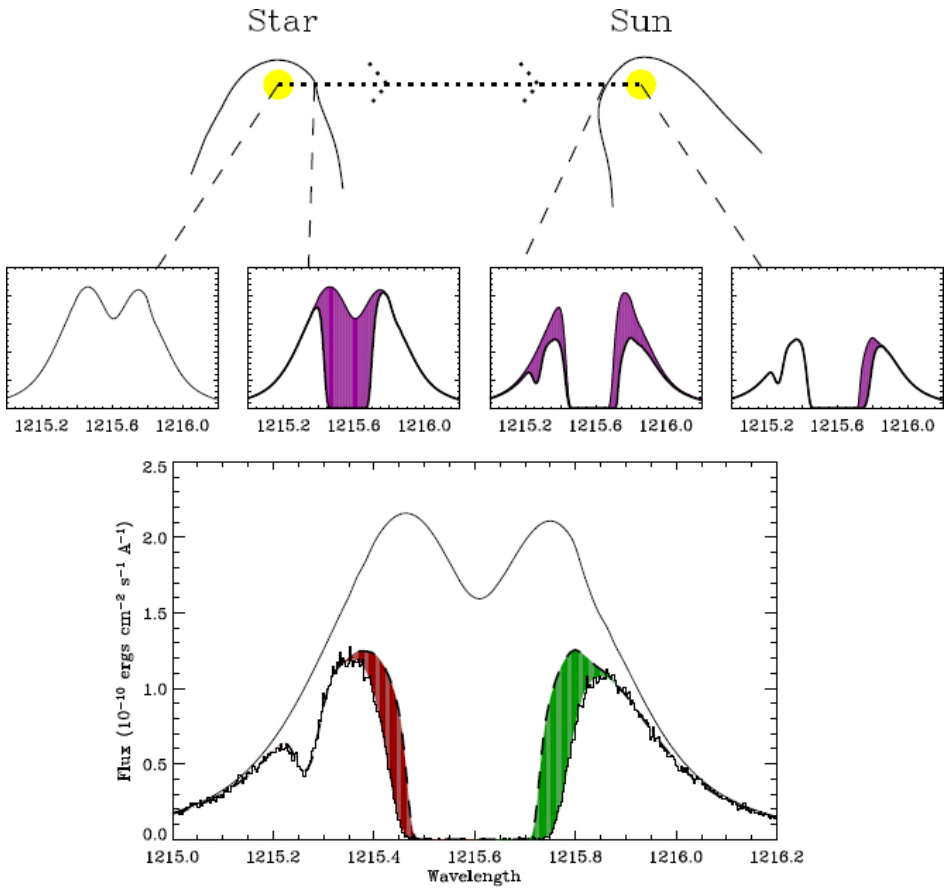

Figure 4.5: A cartoon showing the path the light from a star takes and the absorbers it encounters before reaching our detectors. The light encounters the astrosphere, then ISM, then heliosphere. The bottom panel of Figure 4.5 shows the observed Ly profile of a Cen B (Linsky & Wood 1996). The green side shows the redshifted heliospheric absorption in green and the blueshifted astrospheric absorption in red. From Wood (2004); Wood et al. (2001).

along the same sight lines are very useful in educating the Ly α fits. They tend to be far less saturated and provide an important constraint on the quantity and location of interstellar absorption features. We employ this technique in our own analysis.

In Figure 5.4, we present and discuss the detection of two new astrospheres around targets GJ3323 and GJ173. The Ly α fit of GJ173 requires an astrospheric component, but GJ3323 fit is trickier because of the noisiness of the data. The fit

without an astrospheric component is acceptable, but because the HD32147 sight line is in close proximity, contains two ISM absorption components (constrained by the Mg II fits), and has data with a higher S/N, we conclude that the GJ3323 emission line most likely requires an astrospheric absorption component.

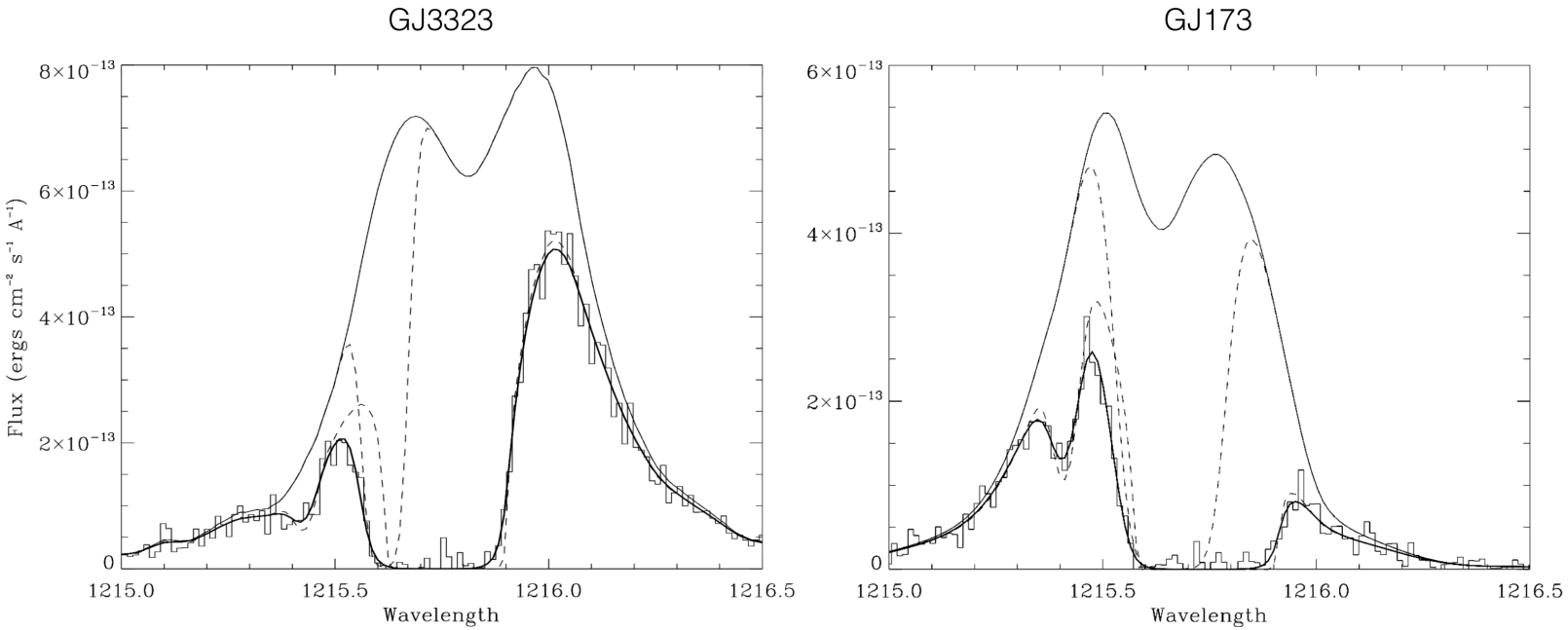

Figure 4.6: Preliminary astrosphere analyses of the Lyman- α emission profile (Brian E. Wood, private correspondence). Two new astrosphere detections were reported for GJ3323 and GJ173. The units along the x-axis are in Angstrom. For both plots, the double peaked line represents the flux background without absorption by the astrosphere or ISM. If you follow this line from left to right, a dashed line comes off of it which represents interstellar absorption. A separate dashed line comes off of the hump at 1215.5 Å in both plots, which accounts for the astrospheric absorption. The thick black line represents the combined absorption fits of both the interstellar and astrospheric components. One can see how well the combination fits the observed spectra. See Wood (2004) for a more detailed explanation of the fitting process

Chapter 5

Conclusion

5.1 Summary of Results

We have presented our analysis of high resolution UV data from *Hubble Space Telescope* along eight sight lines to reconstruct LISM cloud morphology along the historical trajectory of our Sun's travel through the Milky Way. We detect Mg II absorption in four sight lines, and Fe II, C II, and O I in one. In the non-detections, the radial velocity of the clouds is too far from the target star's or the signal to noise is too low to see absorption.

In four sight lines, we identify three different discrete clouds: the LIC (four sight lines), Aur (two sight lines), and Blue (two sight lines). The presence of the LIC in all four sight lines supports other studies that suggest we are currently contained within LIC material. Our range of column density measurements, even in the small area of the sky we survey, shows the LIC does not have a homogeneous density throughout, and that the small scale structure of the LIC is most likely very complex. This highlights the importance of dense surveys of the sky, which can impact how we think of the morphology of this material.

Based on these measurements in conjunction with cloud edge borders calculated in Redfield & Linsky (2008), we expect for the past ∼4--5 million years, the Sun has been traveling through hot, low density Local Bubble material, and only

recently (∼140,000 years ago) entered the warm, partially ionized clouds of LISM. In our model, we assume the boundaries of the LIC, Aur, and Blue are in close proximity, and their traversal could have caused a series of heliospheric expansions and contractions. Encounters with the Blue and Aur clouds likely compressed the heliospheric boundaries to the distances at which they exist today. When in the Local Bubble material, the lack of density would have allowed the heliopause to expand well beyond its contemporary boundaries, where it would have remained stable.

In our recent travels, it is highly unlikely the heliosphere would have been contracted to the extent that the boundaries would have reached any of the inner planets in the solar system, much less 1 AU. This would require an extreme density difference in one of the nearby LISM clouds we traversed, which is unlikely as we expect the local clouds have similar characteristics to the LIC. The Blue and Aur clouds may not have the exact same volume densities to the LIC, but it would take extreme changes in velocity or density to push the heliospheric boundaries inward to any great extent.

The analysis of our most recent interstellar environment highlights its diversity even over a short period of time. We live in an extraordinary time for the study of the LISM. We can actively measure constituents of the LISM entering our solar system, have spacecraft returning data from beyond the edge of our solar system through the *Voyager* mission, and are on the cusp of transitioning into a new interstellar environment. It is exciting to think that even as soon as 4000 years, we may be exciting the LIC and actively seeing a change in heliospheric boundary conditions (with great hope we are still around). One can only imagine what the galaxy holds in store for our solar system as it keeps running its long laps around the Milky Way. Regardless of what the future holds for humanity, as we look to

the future it is comforting to know that whatever the Milky Way throws our way, the Sun will be close by, continuing to be our first line of defense.

5.2 Future Work

There is more work to be done to increase the comprehensiveness of our results. An analysis of upper limits on column density is certainly something we can achieve in the future. For sight lines we observed Mg II absorption but not Fe II, we can still extract an upper limit for the column density because we know the velocity range where absorption features are present. We fit the Fe II spectra with varying column densities over the wavelength range where absorption features are present in the Mg II data, essentially teasing out the hidden absorption features from the noise. As long as the absorption feature we create is not outside the noise, it will not be an overestimate of the column density contained in the spectra.

We have a view of stellar/cloud movement from Galactic north, but viewing their movement from different vantage points (Galactic east, west, south) and incorporating 3-D models of the LIC, Blue, and Aur clouds will give a more robust representation of the environment we traversed, and a more accurate timeline of travel and in turn heliospheric response over the past $\sim$4--5 million years.

Our understanding of the LISM is far from complete, and the best way to learn more is analyzing as many sight lines as possible. By doing so, we can further refine our understanding of the similarities and differences between the local clouds by defining extremely important characteristics column density, velocity, temperature, and turbulent velocity. More density measurements will lead to further refinement of cloud borders and put tighter constraints three dimensional model of our different clouds. Further, The ISM is a building block of galactic evolution,

so the more we understand about the local environment, the more we can extend that to characterize other parts of the galaxy, leading to a better understanding of galactic evolution as a whole.

Bibliography

Bostroem, K. A., & Proffitt, C. 2011, STIS Data Handbook v. 6.0

Breitschwerdt, D., & de Avillez, M. A. 2006, , 452, L1

Carslaw, K. S., Harrison, R. G., & Kirkby, J. 2002, Science, 298, 1732

de Avillez, M. A., & Breitschwerdt, D. 2007, , 665, L35

Dehnen, W., & Binney, J. J. 1998, , 298, 387

Dupuis, J., Vennes, S., Bowyer, S., Pradhan, A. K., & Thejll, P. 1995, , 455, 574

Frisch, P. C. 1995, , 72, 499

Frisch, P. C. 2006, Solar Journey: The Significance of our Galactic Environment for the Heliosphere and Earth (Springer)

Frisch, P. C., et al. 2013, Science, 341, 1080

Frisch, P. C., & Mueller, H.-R. 2011, Space Science Reviews, 176, 2134

Frisch, P. C., Redfield, S., & Slavin, J. D. 2011, , 49, 237

Frisch, P. C., & York, D. G. 1983, , 271, L59

Fuchs, B., Breitschwerdt, D., de Avillez, M. A., Dettbarn, C., & Flynn, C. 2006, , 373, 993

Gaia Collaboration. 2018, VizieR Online Data Catalog, I/345

Gayley, K. G., Zank, G. P., Pauls, H. L., Frisch, P. C., & Welty, D. E. 1997, , 487, 259

Genova, R., Molaro, P., Vladilo, G., & Beckman, J. E. 1990, , 355, 150

Gloeckler, G., et al. 2004, , 426, 845

Gurnett, D. A., Kurth, W. S., Burlaga, L. F., & Ness, N. F. 2013, Science, 341, 1489

Izmodenov, V., Wood, B. E., & Lallement, R. 2002, Journal of Geophysical Research: Space Physics, 107, SSH 13

Kawaler, S. D. 2015, in Astronomical Society of the Pacific Conference Series, Vol. 493, 19th European Workshop on White Dwarfs, ed. P. Dufour, P. Bergeron, & G. Fontaine, 65

Konow, F., Redfield, S., & Linsky, J. 2020, in American Astronomical Society Meeting Abstracts, American Astronomical Society Meeting Abstracts, 368.07

Lallement, R., Welsh, B. Y., Vergely, J. L., Crifo, F., & Sfeir, D. 2003, , 411, 447

Linsky, J. L., et al. 2006, , 647, 1106

Linsky, J. L., Redfield, S., & Tilipman, D. 2019, The Astrophysical Journal, 886, 41

Linsky, J. L., & Wood, B. E. 1996, , 463, 254

Malamut, C., Redfield, S., Linsky, J. L., Wood, B. E., & Ayres, T. R. 2014, The Astrophysical Journal, 787, 75

McComas, D. J., et al. 2015, , 220, 22

McKee, C. F., & Ostriker, J. P. 1977, , 218, 148

Morton, D. C. 1991, , 77, 119

—. 2003, , 149, 205

Muller, H., Frisch, P. C., Florinski, V., & Zank, G. P. 2006, The Astrophysical Journal, 647, 14911505

Müller, H. R., Frisch, P. C., Fields, B. D., & Zank, G. P. 2009, , 143, 415

Pavlov, A. A., Toon, O. B., Pavlov, A. K., Bally, J., & Pollard, D. 2005, , 32, L03705

Perryman, M. A. C., et al. 1997, , 500, 501

Rebassa-Mansergas, A., Gänsicke, B. T., Schreiber, M. R., Koester, D., & Rodríguez-Gil, P. 2010, , 402, 620

Redfield, S. 2006, Astronomical Society of the Pacific Conference Series, Vol. 352, The Local Interstellar Medium, ed. S. J. Kannappan, S. Redfield, J. E. Kessler-Silacci, M. Landriau, & N. Drory, 79

Redfield, S., & Linsky, J. L. 2000, , 534, 825

—. 2002, , 139, 439

—. 2004, , 613, 1004

—. 2008, , 673, 283

Schönrich, R., Binney, J., & Dehnen, W. 2010, , 403, 1829

Shapley, H. 1921, Journal of Geology, 29, 502

Snowden, S. L., et al. 1997, , 485, 125

Wood, B. E. 2004, Living Reviews in Solar Physics, 1, 2

Wood, B. E., Alexander, W. R., & Linsky, J. L. 1996, , 470, 1157

Wood, B. E., Redfield, S., & Linsky, J. L. 2001, arXiv e-prints, astro

Wood, B. E., Redfield, S., Linsky, J. L., Müller, H.-R., & Zank, G. P. 2005, , 159, 118

Wyman, K., & Redfield, S. 2013, The Astrophysical Journal, 773, 96

Yaqoob, T. 2012, Exoplanet Research Paper Statistics and Sociology (New Earth Labs (Education and Outreach))

Zachary, J., Redfield, S., Linsky, J. L., & Wood, B. E. 2018, , 859, 42

Zachos, J., Pagani, M., Sloan, L., Thomas, E., & Billups, K. 2001, Science, 292, 686

Zank, G. P., & Frisch, P. C. 1999, , 518, 965

Zank, G. P., Pauls, H. L., Williams, L. L., & Hall, D. T. 1996, , 101, 21639